

Physical conditions in the central molecular zone inferred by H_3^+

Franck Le Petit¹, Maxime Ruaud^{2,3}, Emeric Bron¹, Benjamin Godard¹, Evelyne Roueff¹, David Languignon¹, and Jacques Le Bourlot^{1,4}

¹ LERMA, Observatoire de Paris, PSL Research University, CNRS, UMR8112, F-92190 Meudon, France
Place J. Janssen, 92190 Meudon, France
e-mail: Franck.LePetit@obspm.fr

² Univ. Bordeaux, LAB, UMR 5804, 33270 Floirac, France

³ CNRS, LAB, UMR 5804, F-33270 Floirac, France

⁴ Univ. Paris-Diderot, Paris 7

Working draft

ABSTRACT

Context. The H_3^+ molecule has been detected in many lines of sight within the central molecular zone (CMZ) with exceptionally large column densities and unusual excitation properties compared to diffuse local clouds. The detection of the (3,3) metastable level has been suggested to be the signature of warm and diffuse gas in the CMZ.

Aims. We aim to determine the physical conditions and processes in the CMZ that explain the ubiquitous properties of H_3^+ in this medium and to constrain the value of the cosmic-ray ionization rate.

Methods. We use the Meudon PDR code in which H_3^+ excitation has been implemented. We re-examine the relationship between the column density of H_3^+ and the cosmic-ray ionization rate, ζ , up to large values of ζ in the frame of this full chemical model. We study the impact of the various mechanisms that can excite H_3^+ in its metastable state. We produce grids of PDR models exploring different parameters (ζ , size of clouds, metallicity) and infer the physical conditions that best match the observations toward ten lines of sight in the CMZ. For one of them, Herschel observations of HF, OH⁺, H₂O⁺, and H₃O⁺ can be used as additional constraints. We check that the results found for H_3^+ also account for the observations of these molecules.

Results. We find that the linear relationship between $N(\text{H}_3^+)$ and ζ only holds up to a certain value of the cosmic-ray ionization rate, which depends on the proton density. A value $\zeta \sim 1 - 11 \times 10^{-14} \text{ s}^{-1}$ explains both the large observed H_3^+ column density and its excitation in the metastable level (3,3). This ζ value agrees with that derived from synchrotron emission and Fe K α line. It also reproduces $N(\text{OH}^+)$, $N(\text{H}_2\text{O}^+)$ and $N(\text{H}_3\text{O}^+)$ detected toward Sgr B2(N). We confirm that the CMZ probed by H_3^+ is diffuse, $n_{\text{H}} \lesssim 100 \text{ cm}^{-3}$ and warm, $T \sim 212\text{--}505 \text{ K}$. This warm medium is due to cosmic-ray heating. We also find that the diffuse component probed by H_3^+ must fill a large fraction of the CMZ. Finally, we suggest the warm gas in the CMZ enables efficient H₂ formation via chemisorption sites as in PDRs. This contributes to enhance the abundance of H_3^+ in this high cosmic-ray flux environment.

Key words. astrochemistry - molecular processes - ISM:molecules

1. Introduction

H_3^+ has been observed in a variety of environments: dense clouds (Geballe & Oka 1996; McCall et al. 1999; Brittain et al. 2004; Gibb et al. 2010), diffuse clouds (McCall et al. 1998; Geballe et al. 1999; McCall et al. 2002, 2003; Indriolo et al. 2007; Indriolo & McCall 2012) and even the nucleus of an extragalactic source (Geballe et al. 2006). A comprehensive review has been recently published (Oka 2013). The cosmic-ray ionization rate can be inferred using H_3^+ (McCall et al. 2002, 2003; Le Petit et al. 2004). Indriolo et al. (2007) and Indriolo & McCall (2012) present an exhaustive study of H_3^+ observations and conclude that, in local diffuse clouds, the cosmic-ray ionization rate¹ ζ presents variations with a mean value equals to $3.5 \times 10^{-16} \text{ s}^{-1}$. The first detection of H_3^+ in the central molecular zone (CMZ) (Geballe et al. 1999) showed a surprisingly large column density. Subsequent detections in the CMZ (Goto et al. 2002; Oka et al. 2005; Goto et al. 2008; Geballe & Oka 2010; Goto

et al. 2011, 2013, 2014) revealed that, in a radius of at least 100 pc around Sgr A*, H_3^+ presents not only large column densities but also a peculiar excitation since it is observable in its (3,3) metastable level lying at 361 K above the ground rotational state (see Fig. 8). Oka & Epp (2004) established that $N(3,3)/N(1,1)$ and $N(3,3)/N(2,2)$ ratios can be used to infer gas density and temperature. They demonstrated that a large fraction of the CMZ must be neutral diffuse warm gas with $n_{\text{H}} < 100 \text{ cm}^{-3}$ and $T \sim 200 - 300 \text{ K}$ (Oka & Epp 2004; Oka et al. 2005; Goto et al. 2008). Two important questions arise from these unusual observations: 1) what is the cosmic-ray ionization rate required to explain these large amounts of H_3^+ ; and 2) what is the heating source responsible for the warm medium. To answer the first question, Oka et al. (2005) and Goto et al. (2008) used a simple analytic relation between $N(\text{H}_3^+)$ and ζ . Oka et al. (2005) concluded that $\zeta \sim (2 - 7) \times 10^{-15} \text{ s}^{-1}$, i.e., a cosmic-ray ionization rate typically ten times higher than in local diffuse clouds. More recently, Yusef-Zadeh et al. (2013) used synchrotron emission and Fe I K α line to constrain ζ . They found $\zeta_1 \sim 5 \times 10^{-15} \text{ s}^{-1}$ with synchrotron emission and

¹ We note ζ the cosmic-ray ionization rate of H₂, expressed in s⁻¹, and ζ_1 the one of H with $\zeta_1 \sim 0.5 \times \zeta$.

10^{-14} s^{-1} with the Fe I $K\alpha$ line. Finally, Herschel observations of OH^+ , H_2O^+ , and H_3O^+ in the CMZ suggest $\zeta_1 \sim 10^{-14} \text{ s}^{-1}$ toward Sgr B2(M) and (N) (Indriolo et al. 2015).

In this paper, we use the Meudon PDR code² (Le Petit et al. 2006) to study the properties of H_3^+ in a medium submitted to a high cosmic-ray ionizing flux and we propose a scenario that explains both the large H_3^+ column densities observed in the CMZ and its excitation in the (3,3) metastable level. In Sect. 2, we examine the relationship between $N(\text{H}_3^+)$ and the cosmic-ray ionization rate for a large range of ζ (from 10^{-17} to 10^{-12} s^{-1}) and various densities. We also study the impact of several processes on H_3^+ abundance, such as the recombination of electrons on grains and H_2 formation mechanisms. In Sect. 3, we present an analysis of H_3^+ excitation based on new H_3^+ excitation collisional rates with H_2 computed by Gómez-Carrasco et al. (2012). We compare these new results to the pioneering study of Oka & Epp (2004). We also study the possibility of H_3^+ excitation by nonthermal processes, such as IR pumping and excitation at formation. In Sect. 4 we present a scenario accounting for both $N(\text{H}_3^+)$ and H_3^+ excitation, as observed in the CMZ. We check that our results are consistent with other observational tracers of cosmic rays: OH^+ , H_2O^+ and H_3O^+ absorptions in the CMZ, synchrotron, and Fe $K\alpha$ line emission. Finally, we compare the various heating and cooling mechanisms in the CMZ according to our model. Our conclusions are summarized in Sect. 5.

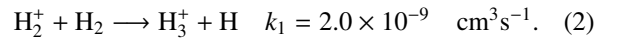
2. Abundance of H_3^+ in diffuse gas

Cosmic-ray ionization is the starting point of chemistries involving H, D, O, and N in diffuse and translucent clouds since these atoms cannot be photoionized by the interstellar radiation field (ISRF), see the review by Grenier et al. (2015). OH and HD have been recognized early (Hartquist et al. 1978; Federman et al. 1996) as potential indicators of the cosmic-ray ionization rate ζ_1 and a value of $\sim 10^{-17} \text{ s}^{-1}$ was derived from the analysis of the column densities of OH and HD found in local diffuse clouds. Recently, Bialy & Sternberg (2015) studied the chemistry of OH for various ζ/n_{H} and low metallicities. Detections of H_3^+ toward various diffuse lines of sight (McCall et al. 2002, 2003; Indriolo et al. 2007; Indriolo & McCall 2012) lead to a significantly larger cosmic-ray ionization rate. This conclusion relies on a simple analytic relation between $N(\text{H}_3^+)$ and ζ derived from the chemical balance between formation and destruction of H_3^+ (see below). More recently, Indriolo et al. (2015) used Herschel observations of OH^+ , H_2O^+ , and H_3O^+ in a sample of Galactic diffuse clouds and inferred a mean value of the cosmic-ray ionization rate in the local medium of $\zeta_1 \sim 1.78 \times 10^{-16} \text{ s}^{-1}$, using the same simple analytic expression based on chemical networks.

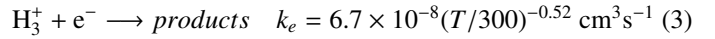
In this section, we revisit the relationship between $N(\text{H}_3^+)$ and ζ and extend it to large values of the cosmic-ray ionization rate, as those may exist in the Galactic center. We also highlight the indirect effect of two processes on $N(\text{H}_3^+)$: the H_2 formation rate and the recombination of electrons on grains.

2.1. $N(\text{H}_3^+)$ vs ζ - the simple analytic expression

The chemical network³ of H_3^+ is simple. Formation of H_3^+ involves the ionization of H_2 by cosmic rays, followed by the reaction of H_2^+ with H_2 :



In diffuse environments, the main H_3^+ destruction reaction is the recombination with electrons,



In dense media, destruction of H_3^+ by CO has to be considered as well.

Assuming this simple chemical network, constant densities, homogeneous medium and integrating over the whole cloud of depth L , the steady state H_3^+ column density $N(\text{H}_3^+)$ is

$$N(\text{H}_3^+) = 0.96 \frac{\zeta L}{k_e} \frac{f}{2 x_e} \quad (4)$$

with f the molecular fraction defined as $2N(\text{H}_2)/N_{\text{H}}$, where $N_{\text{H}} = N(\text{H}) + 2 \times N(\text{H}_2)$ and with $x_e = n(\text{e}^-) / n_{\text{H}}$ the electronic fraction.

If the molecular fraction, electronic fraction, and gas temperature are known or can be guessed, one may deduce $\zeta \times L$ from the measure of $N(\text{H}_3^+)$. In local diffuse and translucent clouds, when available, the molecular fraction is derived from observations in absorption of H and H_2 in the far UV, and the gas temperature is deduced from the ratio of the two first H_2 rotational levels $J=0$ and $J=1$ (Rachford et al. 2002). The electronic fraction is usually assumed to be given by $n(\text{C}^+)/n_{\text{H}}$. This expression has been extensively used by McCall et al. (2002, 2003); Indriolo et al. (2007, 2010); Indriolo & McCall (2012) to deduce ζ in local diffuse clouds. The conclusion of these studies is $\zeta \sim 1.7 \times 10^{-16} - 1.1 \times 10^{-15} \text{ s}^{-1}$ (Indriolo & McCall 2012) in diffuse clouds, a significantly larger value than previously deduced from OH and HD observations. On the other hand, a detailed simulation with the Meudon PDR code of the diffuse line of sight toward ζ Persei, where OH, HD, and H_3^+ have been detected concomitantly, leads to a value of the cosmic-ray ionization rate of $2.5 \times 10^{-16} \text{ s}^{-1}$ (Le Petit et al. 2004), whereas the simple analytic derivation restricted to the analysis of H_3^+ concluded to a value of $\sim 1.2 \times 10^{-15} \text{ s}^{-1}$ (McCall et al. 2003). The value obtained by Le Petit et al. (2004) relies on the modeling of 18 species detected toward ζ Persei with the Meudon PDR code (Le Petit et al. 2006) and the Paris-Durham shock code (Flower & Pineau des Forets 1998). One major constraint is $N(\text{OH})$, which is also proportional to ζ , so that the high value of ζ derived by McCall et al. (2003) leads to a column density of OH that is too large compared to observations (Felenbok & Roueff 1996; Roueff 1996).

Equation 4 has also been used to infer $\zeta \times L$ toward various sources located in the CMZ (Oka et al. 2005; Goto et al. 2008, 2011). Very restricted molecular information is available for these lines of sight, however; the molecular fraction is unknown and the electronic fraction is still assumed to be $n(\text{C}^+)/n_{\text{H}}$. Assuming $f = 1$, an order of magnitude of $\zeta \sim (2-7) \times 10^{-15} \text{ s}^{-1}$ is estimated by Oka et al. (2005).

³ All reaction rates used in this paper come from KIDA database <http://kida.obs.u-bordeaux1.fr> (Wakelam et al. 2012) and the 2012 edition of the UMIST database <http://udfa.ajmarkwick.net>.

² The Meudon PDR code is available at <http://ism.obspm.fr>

2.2. $N(\text{H}_3^+)$ vs ζ relationship - numerical models

In this section, we test Eq. 4 with the Meudon PDR code (Le Petit et al. 2006) for diffuse cloud conditions. We consider different diffuse clouds defined by their total visual extinctions, $A_V^{\text{max}} = 1$, proton densities (three densities are considered, $n_{\text{H}} = 50, 100$, and 1000 cm^{-3}), and illuminated on both sides by the isotropic ISRF expressed in Mathis units (Mathis et al. 1983). The gas temperature is computed at each position in the cloud taking detailed cooling and heating mechanisms into account (photoelectric effect, cosmic-ray heating, exothermic reactions, ...), as described in Le Petit et al. (2006) and Gonzalez Garcia et al. (2008). Our chemical network includes 165 species linked by 2850 chemical reactions. The code computes stationary state chemical abundances at each position using photodestruction rates determined by the radiative transfer and gas temperature computed by the thermal balance. Then, column densities are computed. To test Eq. 4 on a wide range of cosmic-ray ionization rate values, we ran models with ζ from 10^{-17} to 10^{-12} s^{-1} . The input parameters are summarized in Tables 1 and 2. We also introduce the metallicity Z as a multiplicative factor of the elemental abundances of heavy elements (C, N, O, S, F, ...) and of grain abundances. In this section, Z is fixed to 1, whereas in Sect. 4, which is dedicated to CMZ conditions, Z is set to 3.

Table 1. Input parameters used in the Meudon PDR code common to all models discussed in Sect. 2.2.

Parameter	Value	Unit / Ref
Geometry	plane-parallel	
Size	$A_V^{\text{max}} = 1$	
Equation of state	isochoric	
Density	50, 100, 1000	cm^{-3}
ISRF scaling factor, G_0	1 (2 sides)	(1)
Cosmic-ray ionization rate, ζ	variable	s^{-1}
Metallicity, Z	1	
Dust extinction curve	mean Galactic	(2)
Mass grain / mass gas	$0.01 \times Z$	(3)
Mass PAH / mass grain	4.6×10^{-2}	(3)
$N_{\text{H}} / E(\text{B}-\text{V})$	$5.8 \times 10^{21} / Z$	$\text{cm}^{-2} \text{ mag}^{-1}$
R_V	3.1	(4)
Grain size distribution	$\propto r^{-3.5}$	(5)
Minimum grain radius	1×10^{-7}	cm
Maximum grain radius	3×10^{-5}	cm

References. (1) Mathis et al. (1983), (2) Fitzpatrick & Massa (1986), (3) Draine & Li (2007), (4) Seaton (1979), (5) Mathis et al. (1977)

Table 2. Elemental abundances. Z is the metallicity.

Element	Elemental abundance	Reference
He	0.1	
C	$1.32 \times 10^{-4} \times Z$	1
O	$3.19 \times 10^{-4} \times Z$	2
S	$1.86 \times 10^{-5} \times Z$	1
N	$7.50 \times 10^{-5} \times Z$	3
F	$1.8 \times 10^{-8} \times Z$	4

References. (1) Savage & Sembach (1996), (2) Meyer et al. (1998), (3) Meyer et al. (1997), (4) Snow et al. (2007)

$N(\text{H}_3^+)$ as a function of ζ is presented in Fig. 1 where each point corresponds to a model. H_3^+ column density increases with ζ only up to a maximum value of the cosmic-ray ionization rate, ζ^{max} . For moderate ζ , the relationship is linear, in agreement with Eq. 4. Using the computed f , x_e , and T , we checked that Eq. 4 gives an extremely good agreement with the numerical model in the linear increasing part. However, when Eq. 4 is used to estimate ζ with observations, the molecular fraction, electronic fraction, and gas temperature may have to be guessed, contrary to our numerical check where they are consistently computed. The maximum of $N(\text{H}_3^+)$, reached at $\zeta = \zeta^{\text{max}}$, depends on the gas density. In these models, the order of magnitude of the maximum of $N(\text{H}_3^+)$ is 10^{15} cm^{-2} . This value depends on the size of the cloud, here $A_V^{\text{max}} = 1$, and on the gas temperature (see below). For cosmic-rays ionization rates higher than (or even close to) ζ^{max} , Eq. 4 is obviously incorrect and cannot be used to deduce ζ from $N(\text{H}_3^+)$. This decrease of H_3^+ column density with the cosmic-ray ionization rate can be understood from the behavior of the molecular and electronic fractions with ζ .

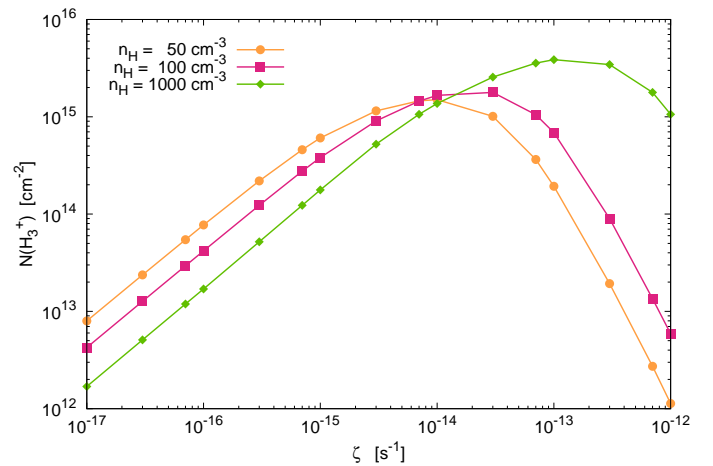


Fig. 1. Column density of H_3^+ as a function of ζ . Each point corresponds to a PDR model as defined in Tables 1 and 2.

Figure 2 shows the computed electronic fraction, $x_e = n(e^-)/n_{\text{H}}$, in the middle of the cloud ($A_V = 0.5$) as a function of ζ . The elemental abundance of C, C/H , is a good proxy for x_e for low values of ζ and for low density clouds (50 and 100 cm^{-3} in our examples). At high cosmic-ray fluxes, x_e is significantly higher than the C/H ratio because a significant amount of electrons is produced by the cosmic-ray ionization of H and H_2 . At high densities and low cosmic-ray fluxes, x_e is lower than the C/H ratio because of efficient neutralization of electrons on grains and PAHs. This point has been discussed by Liszt (2003, 2006).

Figure 3 illustrates the decrease of the molecular fraction with ζ . The lower the density of the gas, the lower the ζ at which this decrease happens. At high flux of cosmic rays, molecular hydrogen is efficiently ionized by cosmic rays and forms H_2^+ , which quickly reacts with electrons to dissociate in hydrogen atoms or reacts with H and H_2 to produce H_2 and H_3^+ . Molecular fractions computed by the PDR code reach values up to 0.9 - 1, whereas FUSE observations of local diffuse clouds show smaller molecular fractions, $f \sim 0.6$ (Rachford et al. 2002). The molecular fractions presented here correspond to single-cloud

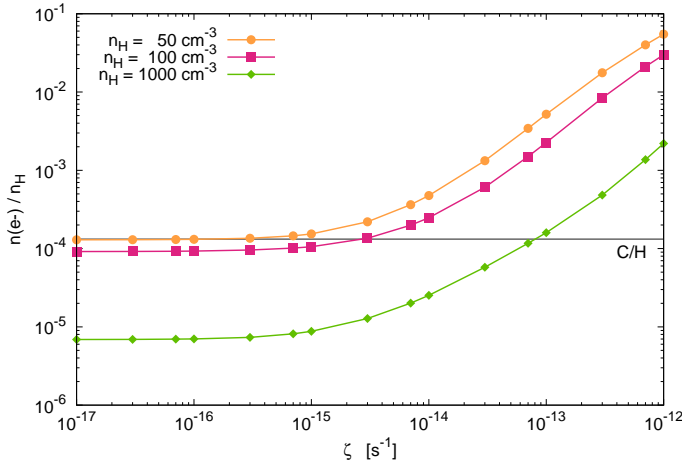


Fig. 2. Computed electronic fraction, x_e , at $A_V = 0.5$ as a function of ζ . Each point corresponds to a PDR model as defined in Tables 1 and 2. The horizontal line represents the elemental abundance of carbon relative to H.

models with a total visual extinction of 1. It is possible that several small components are present on FUSE lines of sight, resulting in a smaller total molecular fraction. This is consistent with a picture of fragmented diffuse interstellar gas (Godard et al. 2014).

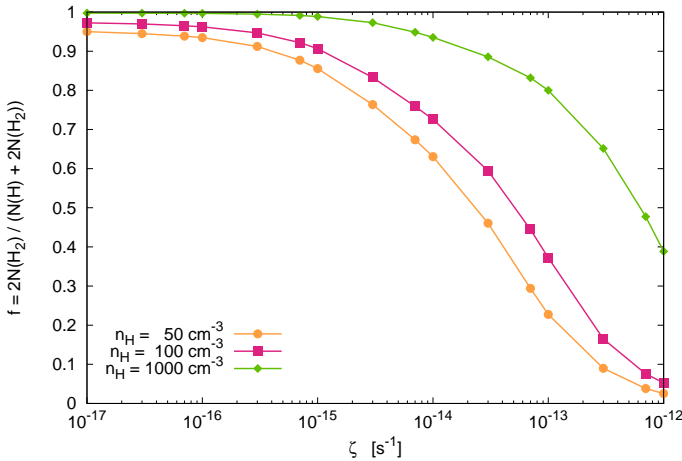
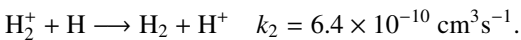
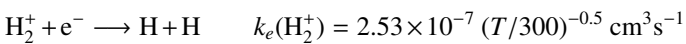


Fig. 3. Molecular fraction f as a function of ζ . Each point corresponds to a PDR model as defined in Tables 1 and 2.

The dependence of $N(\text{H}_3^+)$ with ζ is then straightforward to understand. When the cosmic-ray ionization rate is large, $N(\text{H}_3^+)$ decreases with ζ , first, because less H_2 is available to form H_3^+ and, second, because H_3^+ recombines efficiently because of a large abundance of electrons produced by cosmic-ray ionization of H and H_2 . A more general relationship between $N(\text{H}_3^+)$ and ζ than Eq. 4 can be obtained taking into account, in the chemical balance, H_2^+ reactions that are important at large ζ :



Then, the column density of H_3^+ in diffuse gas is written

$$N(\text{H}_3^+) = 0.96 \times \frac{\zeta L}{k_e} \frac{f}{2x_e} \left[1 + \frac{2k_e(\text{H}_2^+) x_e}{k_1 f} + \frac{2k_2}{k_1} \left(\frac{1}{f} - 1 \right) \right]^{-1} \quad (5)$$

A similar equation is given by Indriolo & McCall (2012) where destruction of H_3^+ by CO is included. Equation 5 shows that, as long as the expression in brackets is close to 1 (low ζ), we recover the linear dependence between the column density of H_3^+ and $\zeta \times L$. However, when dissociative recombination of H_2^+ and charge transfer with H compete with destruction of H_2^+ by H_2 , Eq. 5 shows that the column density of H_3^+ is reduced compared to the prediction of Eq. 4.

Cosmic-ray ionization rates can thus only be deduced with the classical analytical expression, Eq. 4, for moderate ζ , as in standard diffuse lines of sight. For large ζ , this relationship fails. A more general expression, appropriate for low and high cosmic-ray fluxes in diffuse environments, is Eq. 5. In both cases, the difficulty to use such analytical expressions is to estimate properly f and x_e .

2.3. Molecular fraction and H_2 formation processes

Because the molecular fraction is a key parameter in the relationship between the cosmic-ray ionization rate and $N(\text{H}_3^+)$, the transition from atomic to molecular gas must be computed properly. The analytic theory of the H- H_2 transition has been described by Sternberg et al. (2014). In diffuse gas, H_2 is destroyed by UV photons via absorption transitions in the Lyman and Werner bands followed by de-excitation in the continuum of the ground electronic state. In the models presented here, this process is computed taking continuum absorption by dust and carbon atoms of the UV radiation field and self-shielding of H_2 lines into account (Le Petit et al. 2006). The formation of H_2 takes place on grains. In numerical models, this can be simulated in very different ways, from simple analytic formulae to very detailed modeling. In most astrochemical models, a mean formation rate of $3 \times 10^{-17} \sqrt{T/100} \text{ cm}^3 \text{ s}^{-1}$ is used. This rate was deduced from Copernicus and FUSE observations of diffuse clouds in the local neighborhood (Jura 1974; Gry et al. 2002). Several studies based on ISO and Spitzer observations showed that this rate is too low to account for H_2 emission lines in PDRs where the gas and the grains are warm (Habart et al. 2004, 2011). One may wonder if the mean formation rate determined in local diffuse lines of sight also applies to the CMZ, where the gas is warm too. Indeed, this mean value hides complex microscopic mechanisms: H adsorption in chemisorption and physisorption sites, migration at the surface of grains and H_2 formation. The mean value also hides the properties of grains and PAHs, such as their composition and temperature. In the Meudon PDR code, several formalisms are implemented to simulate H_2 formation on grains: analytic expression (Le Petit et al. 2006), moment equation formalism (Le Petit et al. 2009), Langmuir-Hinshelwood (LH) and Eley-Rideal (ER) mechanisms (Le Bourlot et al. 2012), and a stochastic approach that considers the impact of grain temperature fluctuations on H_2 formation rate (Bron et al. 2014).

In all models presented here, the H_2 formation rate is computed using the formalism described in Le Bourlot et al. (2012), i.e., we take into account adsorption in physisorption and chemisorption sites with H_2 formation via LH and ER mechanisms⁴. We upgraded the grain model assuming the grain size distribution contains a log-normal PAH component

⁴ We have not used the most sophisticated H_2 formation model at our disposal (Bron et al. 2014), which takes the effect of grain temperature fluctuations on H_2 formation into account because it is too CPU time

(Compiègne et al. 2011) plus a MRN power law (Mathis et al. 1977) for amorphous carbons and silicates with minimum and maximum radius equal to 10^{-7} and 3×10^{-5} cm. H_2 formation rate on PAHs is not well known, but several laboratory experiments show that the process is efficient (Boschman et al. 2012; Mennella et al. 2012). Here, we assume that ER mechanism on PAHs is as efficient as on grains. As emphasized in Le Bourlot et al. (2012), the efficiency of the LH mechanism depends on grain temperatures whereas the efficiency of the ER mechanism depends on the gas temperature. Indeed, only H atoms with sufficient kinetic energy can reach chemisorption sites. In our models, we assume a threshold of 300 K to reach these sites. This low value accounts for the likely presence of defects on grain surfaces.

To study the sensitivity of the computed molecular fraction to the H_2 formation model, we ran the same models as in the previous section with two prescriptions for the H_2 formation rate on grains: the crude approximation, $3 \times 10^{-17} \sqrt{(T/100)} \text{ cm}^3 \text{ s}^{-1}$, and the more physical model taking ER and LH mechanisms into account. Grain and PAH properties in the CMZ are poorly known. Since they affect the photoelectric heating and ionization degree through ions and electrons recombination and H_2 formation, we also ran models with and without the PAH component. Computed f as a function of ζ are presented for the $n_{\text{H}} = 100 \text{ cm}^{-3}$ models in Fig. 4. In models with fixed H_2 formation rate, the molecular fraction does not depend on the grain surface. There is only a slight f increase at high ζ (between PAH and no PAH models) because of an increase of the gas temperature and variations of the available grain surface for charge recombinations. On the other hand, the consideration of ER mechanism leads to significantly higher molecular fractions at high ζ than the $3 \times 10^{-17} \sqrt{(T/100)}$ approximation.

Figure 5 shows the gas temperature averaged over positions, $\langle T \rangle$, for all models presented in Sect. 2.2. For $\zeta < 10^{-15} \text{ s}^{-1}$ and diffuse conditions ($n_{\text{H}} \leq 100 \text{ cm}^{-3}$), $\langle T \rangle$ is $\sim 60 \text{ K}$, in agreement with FUSE observations (Rachford et al. 2002). Increasing ζ from 10^{-17} to 10^{-12} s^{-1} increases the gas temperature from 60 to 1200 K in models with $n_{\text{H}} = 100 \text{ cm}^{-3}$. In models with a large value of ζ , cosmic rays heat the gas to several hundred Kelvin, firstly, by direct ionization of H and H_2 , followed by thermalization of electrons with the gas; and, secondly, because electrons recombine in exothermic dissociative recombination reactions (mostly the $\text{H}_3^+ + e^-$ reactions with $\Delta E = 4.7 \text{ eV}$ in the three body dissociation). In our models, we assume that each cosmic-ray ionization contributes to the heating of the gas by 4 eV. Usually, formation of H_2 via chemisorbed H atoms is efficient only in photodominated regions, where the temperature of the gas reaches several hundred Kelvin. In typical diffuse clouds, where the gas is at $\simeq 60 \text{ K}$ (Rachford et al. 2002), this process is unlikely. The situation may be different for diffuse gas in the CMZ for which Oka & Epp (2004) suggested that the temperature is several hundred Kelvin, enough to provide the kinetic energy for H atoms to reach chemisorption sites and increase the H_2 formation rate by a significant amount compared to local diffuse clouds.

consuming. Nevertheless, we checked that grain temperature fluctuations do not have a strong effect on our conclusions.

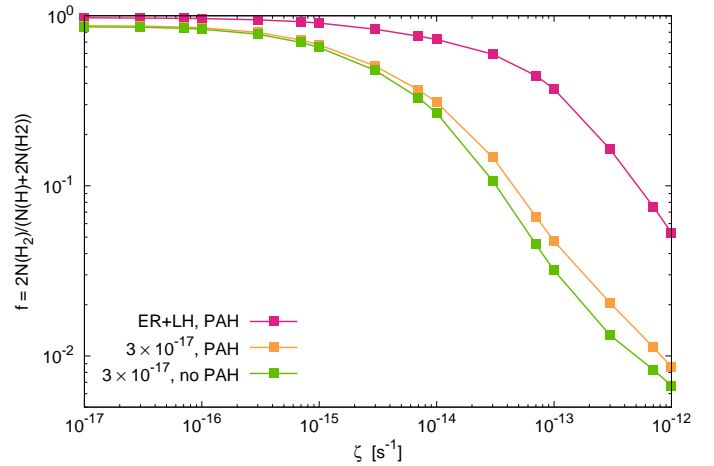


Fig. 4. Molecular fraction as a function of ζ for different grain distributions and H_2 formation mechanisms. Each point corresponds to a PDR model as defined in Tables 1 and 2 with $n_{\text{H}} = 100 \text{ cm}^{-3}$.

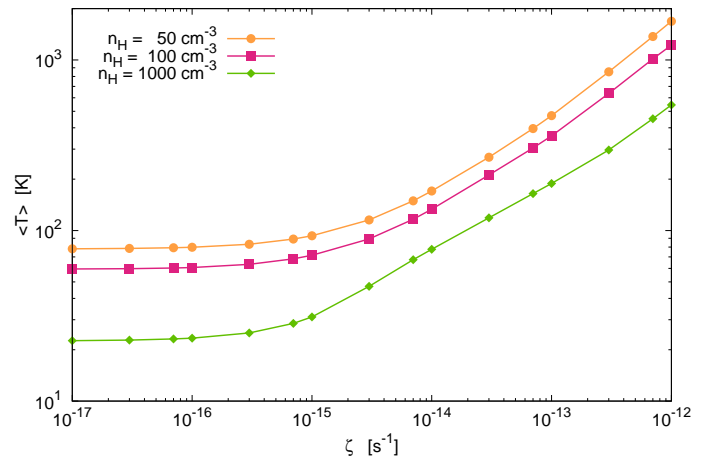


Fig. 5. Mean gas temperature for all models presented in Sect. 2.2. Each point corresponds to a PDR model as defined in Tables 1 and 2.

2.4. Electronic fraction and e^- recombinations on grains

The second important parameter in deriving ζ from H_3^+ observations is the electronic fraction (cf. Eqs. 4 and 5). We showed that, at high cosmic-ray flux, electrons produced by ionization of H and H_2 cannot be neglected compared to those produced by UV ionization of carbon and grains.

Figure 6 presents x_e as a function of ζ for the previous $n_{\text{H}} = 100 \text{ cm}^{-3}$ models. The H_2 formation formalism has only a small impact on x_e . On the contrary, grain surface has a strong impact on x_e . The higher the available grain surface to recombine electrons, the lower the electronic fraction. We do not know the grain properties in the CMZ. In our comparison of models to CMZ observations, we assume a standard grain size distribution plus a PAH component, as described in Sect. 2.2 and 2.3 and we scale the grain mass with the metallicity in the CMZ.

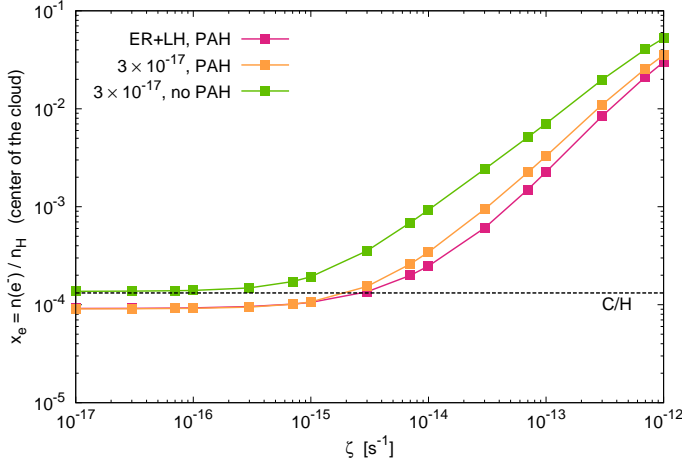
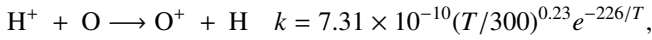


Fig. 6. Electronic fraction as a function of ζ for different grain distributions and H_2 formation mechanisms. Each point corresponds to a PDR model as defined in Tables 1 and 2 with $n_{\text{H}} = 100 \text{ cm}^{-3}$.

2.5. Effect of the gas temperature

Warm gas contributes to increase the abundance of H_3^+ (Le Petit et al. 2004). First, as described above, it increases H_2 formation rate by ER mechanism on chemisorption sites. The available H_2 may lead to the formation of H_3^+ . Second, the dissociative recombination rate of H_3^+ decreases with T . Third, at T above 100 K, the charge exchange reaction between O and H^+ becomes efficient, i.e.,



with k in $\text{cm}^3 \text{ s}^{-1}$. This opens the chemical network of oxygen hydride ions OH^+ , H_2O^+ , and H_3O^+ formed through successive reactions with H_2 . An increase of the densities of these hydrides provides additional channels for electrons consumption. Hence, at large temperatures, electrons have several ways to recombine efficiently in competition with H_3^+ recombination. Moreover, it is then not surprising to find similar velocity profiles in H_3^+ and H_2O^+ spectra obtained in two nearby CMZ sources, the ι star in the Galactic center and Sgr B2 (Schilke et al. 2013), as emphasized by Oka (2015). We specifically discuss the link between H_3^+ and oxygen hydride ions in Sect. 4.2. As a result of these temperature dependence effects on H_3^+ , it is also less surprising to observe large H_3^+ column densities in the warm diffuse gas of the CMZ.

2.6. Conclusion on $N(\text{H}_3^+)$ and ζ

To summarize the effect of H_2 formation prescription and grain / PAHs properties, Fig. 7 presents the dependence of $N(\text{H}_3^+)$ on ζ for the $n_{\text{H}} = 100 \text{ cm}^{-3}$ models. The position of the maximum of the $N(\text{H}_3^+) - \zeta$ relationship depends strongly on the H_2 formation prescription and on grain / PAHs characteristics. A too simplistic recipe, such as the $3 \times 10^{-17} \sqrt{T/100}$ value, leads to erroneous conclusions when trying to deduce ζ from H_3^+ observations for high values of ζ . This illustrates the crucial need, in interstellar chemical studies, to account for detailed microphysical processes.

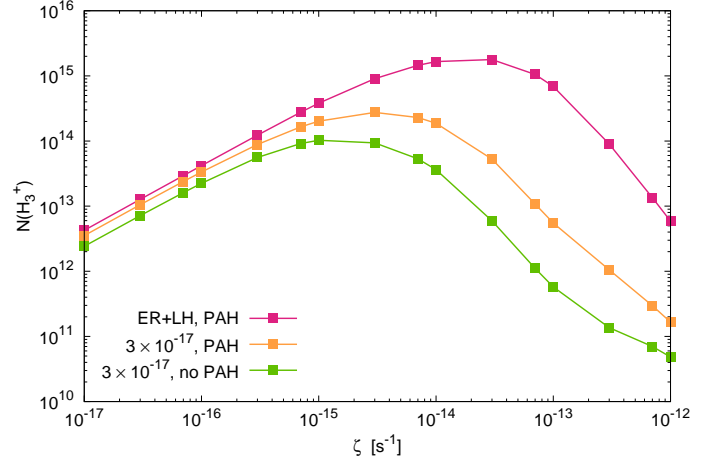


Fig. 7. $N(\text{H}_3^+)$ as a function of ζ for the two H_2 formation models ($3 \times 10^{-17} \sqrt{T/100} \text{ cm}^3 \text{ s}^{-1}$ and Langmuir-Hinshelwood plus Eley-Rideal mechanisms) and two grain distributions: MRN-like distribution and MRN-like + PAH distribution. For all models $n_{\text{H}} = 100 \text{ cm}^{-3}$.

3. H_3^+ excitation

Gas density and temperature in diffuse gas can be inferred from H_3^+ observations in states (3,3), (2,2), and (1,1) (Oka & Epp 2004). Geballe (2012) stated that $N(3,3)/N(1,1)$ is a good thermometer for any temperature and $N(3,3)/N(2,2)$ is a good densimeter for high temperature; see discussion in Oka (2013). Oka & Epp (2004) computed maps of these ratios in the plane $n(\text{H}_2) - T$ and deduced that the gas probed by H_3^+ in the CMZ is diffuse ($n(\text{H}_2) \leq 70 \text{ cm}^{-3}$) and warm ($T \geq 300 \text{ K}$). Their computation takes radiative de-excitations and collisional excitation and de-excitation with H_2 into account. As H_3^+ collision rates were not available, Oka & Epp (2004) proposed an expression based on the Langevin expression with proper account of microreversibility. Recent theoretical studies have been performed on the $\text{H}_3^+ - \text{H}_2$ system. First, Hugo et al. (2009) computed reactive and nonreactive collision rates for temperatures below 50 K with a strong ergodicity and full nuclear spin scrambling hypothesis. Second, Gómez-Carrasco et al. (2012) extended the temperature range up to 500 K and used a dynamically biased statistical model coupled to a recent global potential energy surface of the H_3^+ system (Aguado et al. 2010). Finally, Park & Light (2007) studied the ortho-para conversion in the $\text{H}_3^+ + \text{H}_2$ reaction.

Apart from thermal processes, two additional excitation mechanisms of the (3,3) metastable level may have to be considered. As reported by Goto et al. (2008), John Black suggested the possibility of IR pumping of the ortho (1,0) that could decay after several transitions in the (3,3) metastable level. Another excitation mechanism could be the formation of H_3^+ in excited states as a result of the exothermic $\text{H}_2^+ + \text{H}_2$ reaction.

In this section, we examine the relevance of various excitation mechanisms and discuss the relationship between H_3^+ excitation and the physical conditions of the gas, temperature, and density. We introduced the various H_3^+ excitation mechanisms in the Meudon PDR code. Radiative data come from Lindsay & McCall (2001) and are available electronically on the website maintained by B. McCall (<http://h3plus.uiuc.edu>). To discuss the uncertainties arising from the uncertainties in the collision rates, we implemented the two sets of collision rates by Oka &

Epp (2004) and Gómez-Carrasco et al. (2012). Whereas Oka & Epp (2004) do not discriminate between ortho and para levels, Gómez-Carrasco et al. (2012) consider the appropriate nuclear spin restrictions and provide state-to-state collision rates for the 24 first levels of H_3^+ with H_2 . We implemented collisions of H_3^+ with H_2 in $v = 0$, $J = 0$ and $v = 0$, $J = 1$ since most of molecular hydrogen molecules are in these low energy states. We always use 24 levels for H_3^+ except in Sect. 3.3 where 54 levels are introduced, as required for our analysis. Collision rates with H and He are derived from those with H_2 $J=0$ with a scaling law involving the reduced mass. Since H_3^+ is coexistent with H_2 , H_2 is the main collisional excitation and de-excitation partner. Collisions with electrons have been studied (Faure & Tennyson 2003; Faure et al. 2006; Kokkoulou et al. 2010) and may contribute to H_3^+ excitation. Because of the electronic potential interaction symmetries, collisional excitation due to electrons may only occur between levels (J,K) with the same values of K. As the (3,3) metastable level is the lowest level with $K = 3$, contribution of electron collisions may only take place via (4,3) de-excitation involving an energy difference of 494 K. In the present study, we did not include those collisions in the excitation balance.

We recall that the Meudon PDR code computes the atomic and molecular structure of a 1D plane-parallel slab of dust and gas. By default, gas and grain temperatures are computed at each position in the cloud taking the various local heating and cooling mechanisms into account in parallel to level excitation of several atoms and molecules responsible for the cooling of the gas. Level excitation is computed by solving the radiative transfer equation as described in Gonzalez Garcia et al. (2008). The PDR code considers collisional excitation and de-excitation, radiative de-excitation, radiative pumping, chemical formation, and destruction. It is also possible to run isothermal models with a fixed gas temperature. This alternative is used in Sect. 3.2 to produce maps in the plane $n_{\text{H}} - T$, which can be compared to Oka & Epp (2004).

3.1. Chemical excitation

The exothermicity of the $\text{H}_2 + \text{H}_3^+$ reaction is 1.7 eV. This energy may be redistributed as kinetic energy of products and internal energy of H_3^+ and can contribute to the excitation of its (3,3) level. This mechanism may be efficient if the timescale associated with the formation-destruction cycle is short compared to other (de)excitation mechanisms. The chemical timescale of H_3^+ is inversely proportional to the product of the destructive recombination rate and H_3^+ density and thus dependent on the cosmic ionization rate. In the center of a stationary diffuse cloud ($n_{\text{H}} = 100 \text{ cm}^{-3}$, ISRF scaling factor $G_0 = 1$, $A_{\text{V}}^{\text{max}} = 1$), we obtain a chemical timescale of about 19 yrs for $\zeta = 10^{-16} \text{ s}^{-1}$ and 2 yrs for $\zeta = 10^{-13} \text{ s}^{-1}$. For comparison, the collisional de-excitation rate of the (3,3) level is found to be ~ 3 yrs and ~ 4 yrs, respectively. Then, chemical excitation may contribute and even dominate H_3^+ excitation at large ζ .

Since H_3^+ excitation at formation is unknown, we consider three different prescriptions :

- *Scenario A*: we assume equipartition of energy, i.e., 33% of the available 1.7 eV are included as internal energy (corresponding to 6510 K). This energy is far above the 24 first energy levels for which excitation rates are available (Gómez-Carrasco et al. 2012). In addition, these excited levels decay

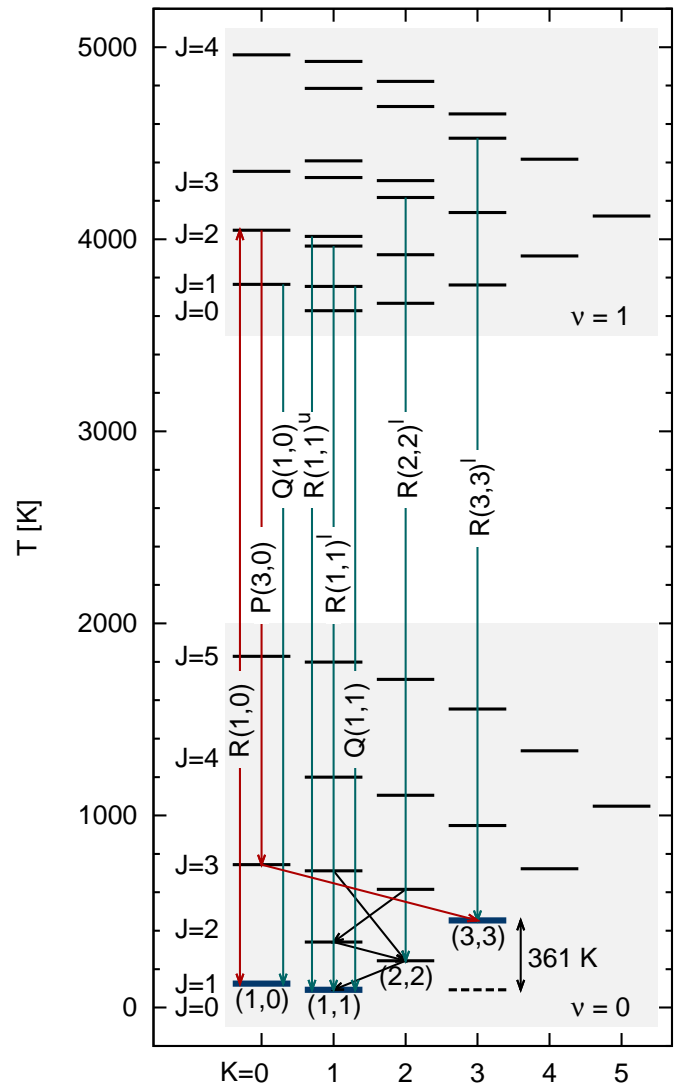


Fig. 8. Schema of H_3^+ levels with the IR pumping mechanism discussed in Sect. 3.3 in red.

radiatively at a rate $\sim 10^{-3} \text{ s}^{-1}$ (Lindsay & McCall 2001), much more efficiently than through any collisional deexcitation process. We then assume that these high levels radiatively cascade toward lower levels and finally contribute to the population of the 24 first levels proportionally to their statistical weights.

- *Scenario B*: H_3^+ is formed following a Boltzmann distribution at gas temperature. This hypothesis assumes the newly formed molecule has time to thermalize with the gas.
- *Scenario C*: formation energy is transferred mainly into kinetic energy and H_3^+ molecules are formed in their para (1,1) / ortho (1,0) ground states, in the ratio of their statistical weights.

Figure 9 shows the $N(3,3)/N(1,1)$ ratios as a function of ζ for the three prescriptions. Results are presented for PDR models with $n_{\text{H}} = 100 \text{ cm}^{-3}$, $A_{\text{V}}^{\text{max}} = 1$, and $G_0 = 1$ and 10. This last value of G_0 corresponds to the order of magnitude of the UV radiation field in the CMZ (Porter & Strong 2005; Moskalenko et al. 2006). In these models, Gómez-Carrasco et al. (2012) collision rates are used.

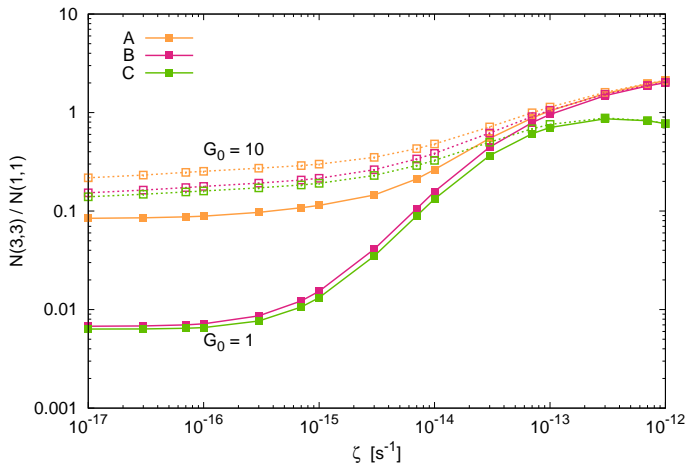


Fig. 9. Ratios $N(3,3)/N(1,1)$ as a function of ζ for three scenarii for H_3^+ excitation at formation. A: 33% of the exothermicity is used as internal energy, B: H_3^+ is formed following a Boltzmann distribution at gas temperature, C: H_3^+ is formed in its two levels (1,1) and (1,0) in a ratio corresponding to their degeneracy. Solid lines correspond to $G_0 = 1$ and dotted lines to $\chi = 10$.

The $N(3,3)/N(1,1)$ ratio exhibits a significant increase for low values of ζ when scenario A is introduced and when $G_0 = 1$. These conditions correspond to a mean kinetic temperature of ~ 65 K for $\zeta = 10^{-16} \text{ s}^{-1}$ so that collisions are not efficient to excite the (3,3) level. However, when $G_0 = 10$ under the same low values of ζ , the mean kinetic temperature increases (T reaches ~ 160 K for $\zeta = 10^{-16} \text{ s}^{-1}$), such that the $N(3,3)/N(1,1)$ ratio also increases significantly. Hence, the additional excitation introduced in scenario A is moderate compared to that in scenarios B and C.

At high ζ , $N(3,3)/N(1,1)$ ratios increase with ζ . In scenario A, the ratio converges toward $14/3$, the ratio of the statistical weights of the (3,3) and (1,1) levels since characteristic timescales for statistical equilibrium are controlled by chemical processes. Models B, with the hypothesis that H_3^+ is formed following a Boltzmann distribution at gas temperature, also converge toward this value. Indeed, the mean gas temperature is then 360 K and 420 K for, respectively, $G_0 = 1$ and 10, and for $\zeta = 10^{-13} \text{ s}^{-1}$, so the Boltzmann distribution at gas temperature tends toward a repartition following statistical weights. Since the gas temperature is high and collisional excitation is efficient, even scenario C gives large values of $N(3,3)/N(1,1)$. Nevertheless, for this scenario, when $\zeta > 10^{-13} \text{ s}^{-1}$, $N(3,3)/N(1,1)$ decreases with ζ because collisional excitations no longer have time to contribute to the excitation from low levels (1,1) and (1,0) before the molecule is destroyed.

These results show the importance of chemical excitation to compute H_3^+ excitation. Fortuitously, this contribution is not as decisive in CMZ conditions ($G_0 \approx 10$ and high flux of cosmic rays) as in typical diffuse clouds because gas temperature becomes high enough to enhance collisional excitations. Values close to 1 have been found for the $N(3,3)/N(1,1)$ ratio in CMZ observations. These values are obtained in Fig. 9 for high values of ζ . This is discussed in Sect. 4. In the following, scenario A is always used except when explicitly said.

3.2. Sensitivity to collisional excitation rates

Collisional excitation of H_3^+ is a significant source of uncertainty in describing the population of excited levels. We check the sensitivity to the available collision rates by running two sets of 176 isothermal and isochoric PDR models, one set with Oka & Epp (2004) prescription and another one with Gómez-Carrasco et al. (2012) collision rates. The proton density is varied from 1 to 10^5 cm^{-3} and the temperature range is between 50 and 1000 K. The Galactic values reported in Tables 1 and 2 are used ($G_0 = 1$, $A_V^{\text{max}} = 1$) with a cosmic-ray ionization rate value $\zeta = 10^{-16} \text{ s}^{-1}$. We also assume that 33% of the exothermicity of the formation reaction excites H_3^+ at formation following scenario A described in Sect. 3.1.

Figure 10 shows corresponding results as contour maps of the ratios $N(3,3)/N(1,1)$ and $N(3,3)/N(2,2)$. First, we obtain similar results to those reported in Oka & Epp (2004) and Oka et al. (2005) when we use their collision rates prescription, even though our models include chemical excitation. Second, we also find that models including Gómez-Carrasco et al. (2012) collision rates suggest slightly higher densities and temperatures than those obtained with Oka & Epp (2004) prescription. This is more apparent in Fig. 11, which presents the space parameter where $N(3,3)/N(1,1) = 0.57 \pm 0.11$ and $N(3,3)/N(2,2) > 3.21$, corresponding to the 2MASS J17470898-2829561 line of sight (Goto et al. 2011). We then conclude that, to the first order, the available collisional excitation rates of H_3^+ (Oka & Epp 2004; Gómez-Carrasco et al. 2012) lead to similar estimates of the density and temperature. In the following, we use Gómez-Carrasco et al. (2012) collision rates, which are calculated from a precise intermolecular potential surface and take nuclear spin restriction rules into account.

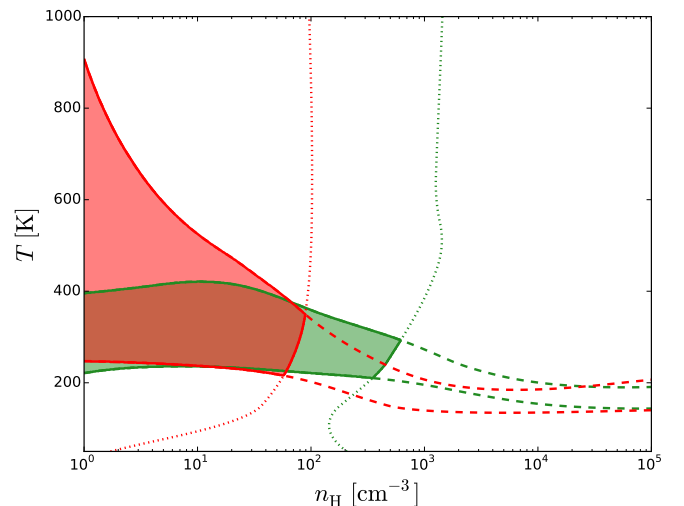


Fig. 11. $N(3,3)/N(1,1)$ (dashed lines) and $N(3,3)/N(2,2)$ (dotted lines) ratios in a plane $n_{\text{H}}-T$ matching observations toward 2MASS J17470898-2829561, Δv between -150 and -60 km s^{-1} (Goto et al. 2011). Red corresponds to models obtained with Oka & Epp (2004) collision rates and green to models obtained with Gómez-Carrasco et al. (2012) collision rates.

Figure 12 presents the same ratios for models with a larger value of ζ , $3 \times 10^{-14} \text{ s}^{-1}$, which is more appropriate for CMZ conditions, as emphasized later. Compared to the previous contour maps, the increase of the cosmic-ray flux enhances the

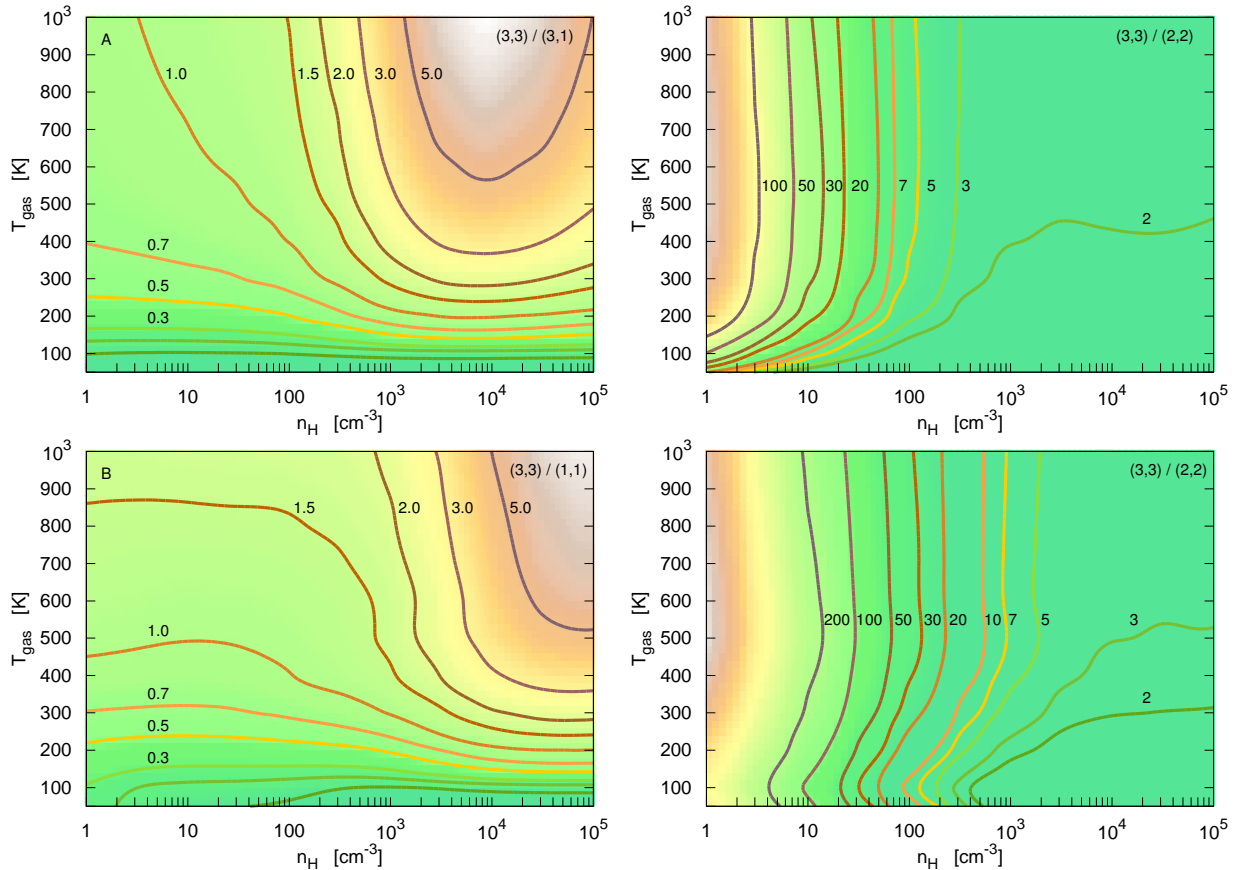


Fig. 10. Ratios $N(3,3)/N(1,1)$ and $N(3,3)/N(2,2)$ in the plane $n_{\text{H}}-T$ obtained with the Meudon PDR code. Top (A): models with Oka & Epp (2004) H_3^+ collision rates. Bottom (B): models with Gómez-Carrasco et al. (2012) collision rates.

$N(3,3)/N(1,1)$ ratio in the low density ($n_{\text{H}} < 100 \text{ cm}^{-3}$) and low temperature ($T < 300 \text{ K}$) domain because of the faster formation-destruction cycle of H_3^+ .

3.3. Excitation by IR pumping

Goto et al. (2008) reported a suggestion by John Black: (3,3) level population may be enhanced by IR pumping (see Fig. 8). Photons at $3.6685 \mu\text{m}$ pump the ortho (1,0) level of the ground vibrational state toward the vibrationally $\nu_2 = 1$ excited state (2,0). This is followed by rapid radiative de-excitation into (3,0) in $2.53 \times 10^{-2} \text{ s}$. Then level (3,0) de-excites toward the (3,3) metastable level through a semiforbidden radiative transition in less than four hours. Goto et al. (2008) estimate that, despite an enhanced IR radiation field in the CMZ compared to local conditions, this process should not be competitive with collisional excitation in the CMZ (see their Sect. 5.5).

To examine the impact of this process, we increase the number of H_3^+ levels considered in the PDR code up to level $\nu = 1, J = 2, K = 0$. We use Gómez-Carrasco et al. (2012) collision rates for the 24 first levels of H_3^+ and Oka & Epp prescription for upper levels. Following Porter & Strong (2005) and Moskalenko et al. (2006), the radiation field in the CMZ at $3.7 \mu\text{m}$ could be 20 times higher than in local ISM. In the Meudon PDR code, the intensity of the incident radiation field in the visible and infrared is modeled by two black bodies: one

corresponding to stars emission and one to dust emission. We scale the intensities of these black bodies so that the intensity in the visible - IR impinging on the slab of gas is 20 times the standard radiation field at the wavelength of the R(1,0) transition.

We ran several models of diffuse clouds with $n_{\text{H}} = 100 \text{ cm}^{-3}$, $A_{\text{V}}^{\text{max}} = 1$ and with different values of G_0 , ζ and incident intensity at $3.6685 \mu\text{m}$ to cover local and CMZ conditions. Table 3 presents $N(3,3)/N(1,1)$ and $N(3,3)/N(2,2)$ for these models. We find that IR pumping always has negligible impact on the $N(3,3)/N(1,1)$ ratio. It has a minor effect on the ratio $N(3,3)/N(2,2)$ in standard conditions. In CMZ conditions, $G_0 = 10$ and $\zeta = 10^{-13} \text{ s}^{-1}$, IR pumping has no effect compared to the other excitation processes (direct collisions and excitation at formation). These models confirm the statement of Goto et al. (2008). In the following of the paper, we neglect this process and use models with 24 H_3^+ levels, allowing us to use consistent collision rates by Gómez-Carrasco et al. (2012).

4. Physical conditions in the CMZ

In this section, we try to constrain the physical conditions and processes in the CMZ, including the cosmic-ray ionization rate. We ran a grid of 1776 isochoric PDR models with parameters relevant to the CMZ conditions. The metallicity, Z , in the CMZ is between 2 and 5 times higher than in the solar neighborhood

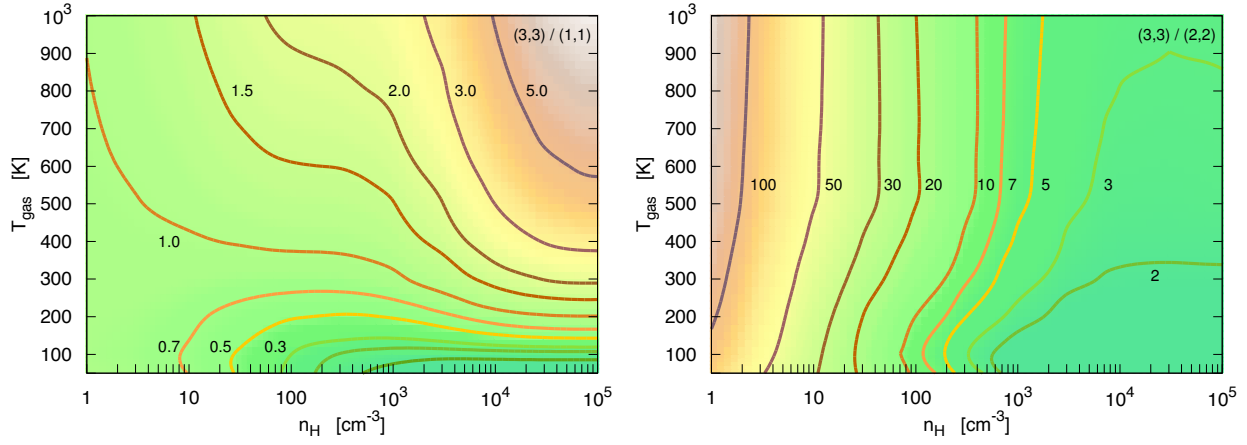


Fig. 12. Same as bottom panels of Fig. 10, but produced with models with $\zeta = 3 \times 10^{-14} \text{ s}^{-1}$.

Table 3. Effect of IR pumping on $N(3,3)/N(1,1)$ and on $N(3,3)/N(2,2)$. The first three columns correspond to input parameters. IR is the scaling factor to the IR part of the ISRF.

G_0	ζ	IR	$N(3,3)/N(1,1)$	$N(3,3)/N(2,2)$
1	10^{-16}	$\times 1$	0.1	7.5
1	10^{-16}	$\times 20$	0.1	5.9
1	10^{-13}	$\times 1$	1.0	9.4
1	10^{-13}	$\times 20$	0.9	7.7
10	10^{-16}	$\times 1$	0.4	8.6
10	10^{-16}	$\times 20$	0.4	8.1
10	10^{-13}	$\times 1$	1.2	8.6
10	10^{-13}	$\times 20$	1.2	8.2

(Rolleston et al. 2000; Daflon & Cunha 2004; Rudolph et al. 2006). We set it to $Z = 3$. This increases elemental and grain abundances as described in Tables 1 and 2. In all models, the incident radiation field in the far-UV impinging on both sides of the cloud is the ISRF scaled by a factor⁵ $G_0 = 10$ (Porter & Strong 2005). The grid of models is divided in five sets of proton densities, $n_H = 10, 20, 50, 100, 1000 \text{ cm}^{-3}$. For each proton density, ζ ranges from 10^{-17} to 10^{-12} s^{-1} , and the size of the clouds, A_V^{max} , ranges from 0.2 to 6. We take the full physics described above into account except for the enhanced IR pumping of H_3^+ , since we found that this process has a negligible effect on H_3^+ excitation. This simplification allows us to limit the computation of H_3^+ excitation to its 24 first levels for which collision rates are reliable. In all models, the gas temperature is computed at each position of the cloud taking heating and cooling mechanisms implemented in the Meudon PDR code into account. For models with constant density, the relationship between the size in cm, L , and the visual extinction, A_V^{max} , is $L = 6.1 A_V^{\text{max}}/Z (100/n_H) \text{ pc}$.

4.1. Estimates of ζ and L with H_3^+

To infer physical conditions on each line of sight where H_3^+ is detected, we use a χ^2 minimization built with H_3^+ column densities in levels (1,1), (3,3), and (1,0) when known. We also check that the best models according to the minimization procedure are compatible with the upper limits on the (2,2)

level. Table 4 summarizes H_3^+ observed column densities on the 10 CMZ lines of sight on which χ^2 minimizations are performed.

Table 4. Observed column densities of H_3^+ in the CMZ in (1,1), (1,0), (3,3), and (2,2) levels. Column densities are expressed in 10^{14} cm^{-2} .

Source	$N(1,1)$	$N(1,0)$	$N(3,3)$	$N(2,2)$
GC IRS 21	28.1 ± 12.3	9.0 ± 4.4	24.2 ± 12.1	< 8.3
GC IRS 3	10.8 ± 2.1	3.4 ± 1.3	8.4 ± 1.9	< 1.6
GC IRS 1W	18.1 ± 3.8	7.9 ± 2.4	11.7 ± 3.0	< 3.3
GCS 3-2	17.0 ± 1.7	4.6 ± 0.8	9.8 ± 1.6	< 3.0
J1743	12.8 ± 1.9	-	5.7 ± 2.2	< 2.1
J1747	6.0 ± 0.7	-	4.3 ± 1.3	< 0.8
NHS 21	8.9 ± 2.2	3.7 ± 1.5	5.6 ± 1.4	< 2.3
NHS 22	16.9 ± 5.6	7.9 ± 3.5	9.7 ± 2.7	< 3.6
NHS 25	11.4 ± 5.9	4.0 ± 3.8	7.4 ± 5.3	< 3.9
NHS 42	17.7 ± 5.1	8.4 ± 4.1	8.6 ± 4.1	< 4.0
Mean	14.5 ± 0.8	6.5 ± 1.1	8.6 ± 1.0	

References. J1747 corresponds to 2MASS J17470898-2829561 and J1743 to 2MASS J17432173-2951430. Data are from Goto et al. (2008) for all lines of sight except for J1747 and J1743 for which data come from Goto et al. (2011). The GCS 3-2 line of sight is not taken into account to compute the weighted mean value (see text).

For all lines of sight, except GCS 3-2, a clear $\chi^2 < 1$ zone is found with models $n_H = 10$ to 100 cm^{-3} (Fig. 13 shows an illustration of the χ^2 minimization for the J1747 line of sight). Models with $n_H = 1000 \text{ cm}^{-3}$ only reach a $\chi^2 < 1$ for GCS IRS 21, NHS 22, and, marginally, in the case of J1747. Moreover, when a χ^2 of 1 is reached for $n_H = 1000 \text{ cm}^{-3}$ models, column densities in the (2,2) level are only lower than the upper limit by a few percent. For these reasons, even if it is formally not possible to reject models with densities of 1000 cm^{-3} , this density is less likely. As expected, we find that the lower the density, the lower the cosmic-ray ionization rate and the larger the size of the cloud. Figure 14 presents a comparison of χ^2 contours for the five densities for the line-of-sight NHS 22.

Table 5 lists, for each line of sight, the positions in the $\zeta - L$ plane where χ^2 values are minimal, as well as the corresponding computed H_3^+ level column densities, molecular fractions, average temperatures, and electronic fractions. Assuming H_3^+ has similar properties on the various lines of sight as demonstrated by Goto et al. (2005, 2008, 2011), we can derive a weighted

⁵ In Sect. 3.3, we tested with the maximal possible value, $G_0 = 20$ to study the possible impact of IR pumping. Here, we use an intermediate value, $G_0 = 10$. This has no impact on the results.

mean of observed column densities (Table 4). This weighted mean is computed assuming the uncertainties in observations are dominated by photon noise and therefore, follow a Poisson process. We exclude from this weighted mean the GCS 3-2 line of sight since it seems peculiar. A χ^2 minimization on this weighted mean leads to a cosmic-ray ionization rate and a path length ranging from 10^{-14} s^{-1} and 66 pc for $n_{\text{H}} = 10 \text{ cm}^{-3}$, to $11 \times 10^{-14} \text{ s}^{-1}$ and 4 pc for $n_{\text{H}} = 100 \text{ cm}^{-3}$ (see Table 5). It is difficult to constrain ζ and L further without additional information about the gas density.

Our value of ζ is somewhat larger than the estimate by Yusef-Zadeh et al. (2013), who deduced from synchrotron and Fe K α observations, $\zeta_1 \sim 10^{-15} - 10^{-14} \text{ s}^{-1}$. However, this value is not incompatible since low-energy cosmic-ray ions may contribute to ionization without producing synchrotron emission and, according to Strong et al. (2010), the luminosity of cosmic-ray protons is ~ 70 times that of cosmic-ray electrons.

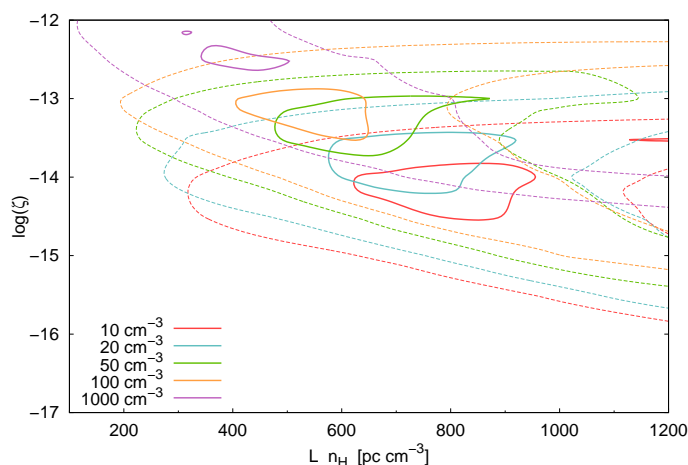


Fig. 14. Comparison of the χ^2 contours for the five densities for the NHS 22 line of sight. Solid lines correspond to $\chi^2 = 1$ and dashed lines to $\chi^2 = 5$.

4.2. Additional constraints: OH^+ , H_2O^+ , H_3O^+ , and HF

Thanks to PRISMAS and HEXOS Herschel key programs, several hydride molecules (HF, CH, OH^+ , H_2O^+ , H_3O^+ , CH^+ , SH^+ , ...) have been observed in absorption toward several lines of sight in the CMZ (Gerin et al. 2010a,b; Neufeld et al. 2010; Godard et al. 2012), but not on the lines of sight where H_3^+ is detected. Nevertheless, the Sgr B2(N) line of sight, part of the HEXOS program, is close to J1747. The projected distance between the two objects is 18 pc (assuming a distance to the Galactic center of 8 kpc). Oka (2015) noticed a strong similarity between H_2O^+ velocity components toward Sgr B2(M) and those of H_3^+ toward J1747, and Indriolo et al. (2015) observe (see their Fig. 4 and 5) similar components between Sgr B2(N) and Sgr B2(M). Figure 15 presents HF and H_3^+ spectra toward Sgr B2 (N) and J1747. Both molecules present similar velocity absorption components. Absorption features associated with the diffuse gas in the CMZ are located between -150 and -60 km s^{-1} (Goto et al. 2011). In this velocity range, HF presents four absorption components, H_3^+ one unresolved (3,3) absorption feature and 3 (1,1) components. In addition, weak CO absorption components are detected. Concerning the other absorption

components, the strong absorption of HF at $v_{\text{LSR}} = 60 \text{ km s}^{-1}$ is related to the Sgr B2(N) complex. Three absorption components due to spiral arms are present at -40 , -20 , and 0 km s^{-1} , deduced from a longitude-velocity map of the CO J=1-0 emission in this region (Oka et al. 2012).

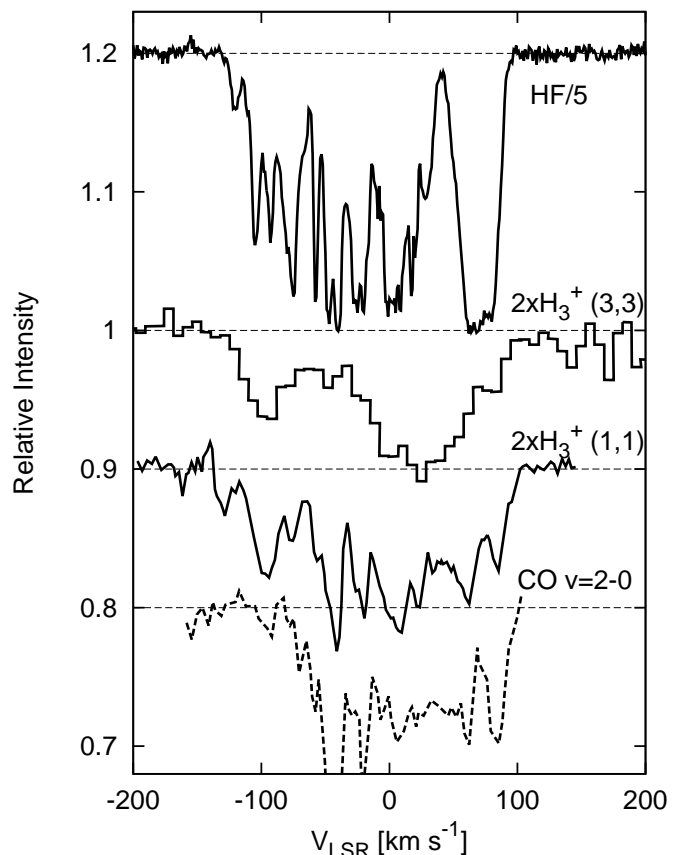


Fig. 15. HF spectrum for the J=1-0 transition obtained with Herschel/HIFI toward Sgr B2(N) (HEXOS key program) and H_3^+ spectrum for the R(3,3) transition (Goto et al. 2011) and for the R(1,1)' (Geballe & Oka 2010) toward J1747. The H_3^+ spectrum of the R(3,3) transition has been corrected by the CO absorption. See Sect. 2 in Goto et al. (2011) for more details.

These similarities in the velocity components between -150 and -60 km s^{-1} may indicate that the size of the diffuse component containing H_3^+ , toward J1747, extends up to the Sgr B2(N) line of sight and, therefore, the size of this component should be at least of $\sim 18 \text{ pc}$. This is also compatible with the fact that H_3^+ is largely observed in the CMZ with always the same peculiar properties, indicating that the filling factor of the neutral diffuse gas probed by H_3^+ must be large. According to Table 5, this leads to $n_{\text{H}} < 50 \text{ cm}^{-3}$ for the J1747 line of sight. As a consequence, the cosmic-ray ionization rate should be $\zeta < 5 \times 10^{-14} \text{ s}^{-1}$.

Assuming that observations toward J1747 and Sgr B2(N) probe the same diffuse gas, derived column densities toward Sgr B2(N) can be used to test our models. We reanalyzed Herschel HF observations. Column densities in the four components between -150 and -60 km s^{-1} are given in Table 6. As discussed by Godard et al. (2012), $N(\text{HF})$ may provide an upper limit to $N(\text{H}_2)$. With an elemental abundance F/H of 1.8×10^{-8} , the value

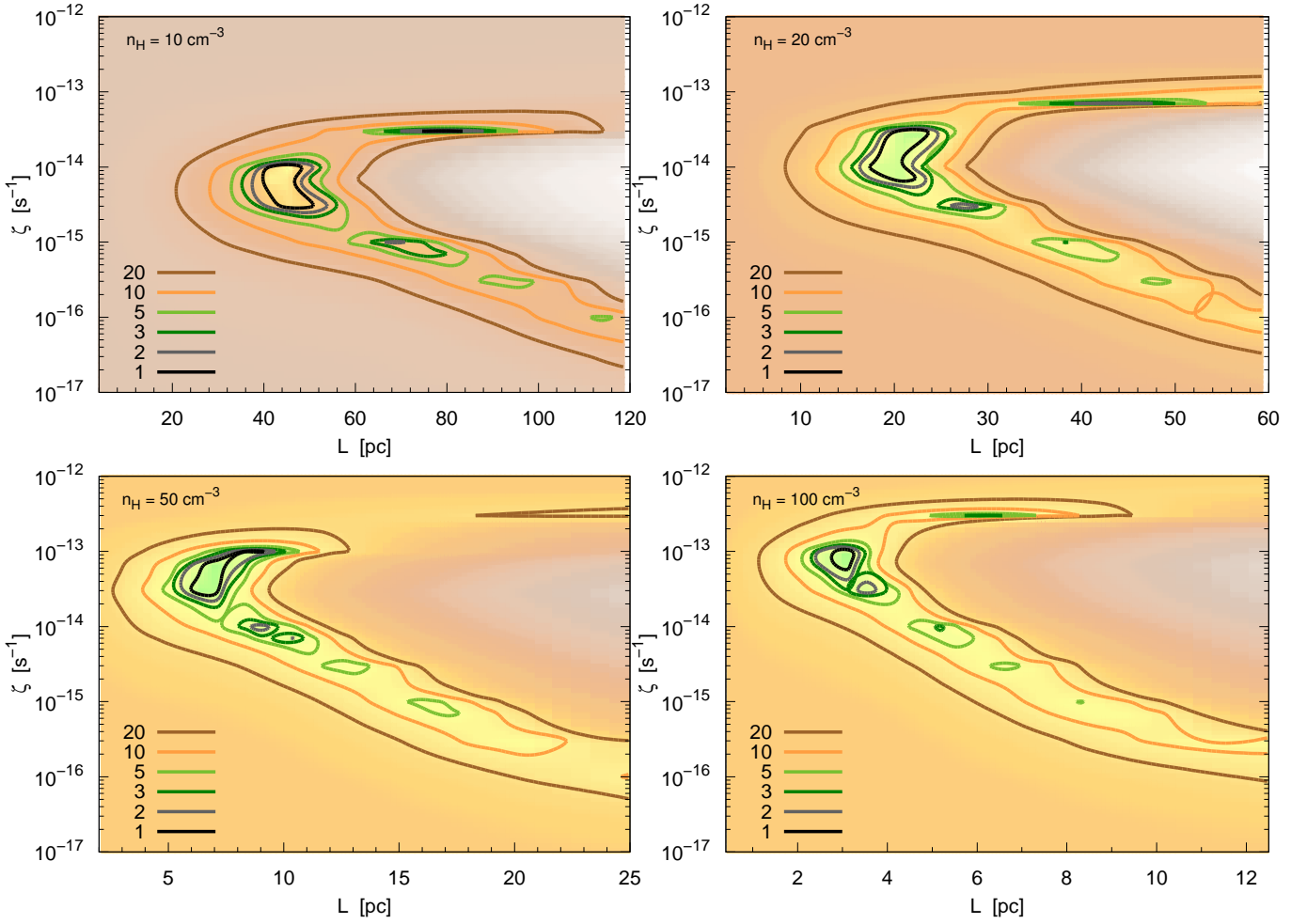


Fig. 13. Contour map of χ^2 using H_3^+ column densities $N(1,1)$ and $N(3,3)$ toward J1747 for the four densities.

in the solar neighborhood, and a molecular fraction of 1, Godard et al. (2012) find $N(\text{HF})/N(\text{H}_2) = 3.6 \times 10^{-8}$ (also reported in Neufeld et al. (2005)). This ratio is only valid for media where $Z = 1$ and where $n(e^-) = n(\text{C}^+)$. To estimate a better ratio in the CMZ, we use Eq. C.3 of Godard et al. (2012) without the hypothesis that the density of electrons is given by C^+ , with $Z = 3$, and with the gas temperature, electron density, and molecular fraction derived from our best models for J1747 (Table 5). We find $N(\text{HF})/N(\text{H}_2) = 1.1 \times 10^{-7}$. Derived $N(\text{H}_2)$ are presented in Table 6.

Table 6. Observed HF and estimated H_2 column densities toward Sgr B2(N).

v_{\min} (km s $^{-1}$)	v_{\max} (km s $^{-1}$)	$N(\text{HF})$ ($\times 10^{13} \text{cm}^{-2}$)	$N(\text{H}_2)$ ($\times 10^{20} \text{cm}^{-2}$)
-150	-114	0.49 ± 0.05	0.4 ± 0.04
-114	-100	2.14 ± 0.65	1.9 ± 0.6
-100	-88	2.15 ± 0.61	1.9 ± 0.5
-88	-60	5.86 ± 0.64	5.3 ± 0.6
-150	-60	10.4 ± 1.7	9.4 ± 1.5

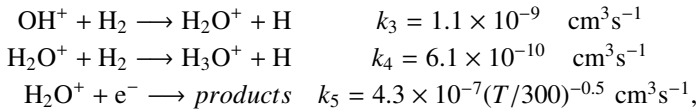
The chemistry of HF is included in the Meudon PDR code. Using our grid of models, we tried a χ^2 minimization built with the column densities of H_3^+ in (1,1), (1,0), and (3,3) toward J1747 and $N(\text{HF})$ toward Sgr B2(N). None of our models

reproduce these four constraints at the same time. When $N(\text{H}_3^+)$, J, K) are reproduced, $N(\text{HF})$ is underpredicted by a factor 4. A possible explanation could be that a fraction of HF observed toward Sgr B2(N) be associated with denser gas than the one probed by H_3^+ (but not too dense either because of the lack of CO absorption in the -150 to -60 km s $^{-1}$ velocity range). On the other hand, the elemental abundance of F is not well understood and is a widely discussed topic. We scaled it by Z but it is possible that F/H does not scale as the other elements (see Abia et al. (2015) and references therein).

The observations of OH^+ , H_2O^+ , and H_3O^+ are particularly interesting since, like H_3^+ , the abundances of these molecules depend on the cosmic-ray ionization rate. Schilke et al. (2010, 2013) report the detection of the H_2O^+ ion toward Sgr B2 with Herschel, whereas Lis et al. (2012, 2014) report H_3O^+ detection. Indriolo et al. (2015) derive their column densities in the different velocity components. With a simple analytic relationship between $N(\text{OH}^+)$ and $N(\text{H}_2\text{O}^+)$, they deduce a value of $\zeta \sim 10^{-14} \text{s}^{-1}$, which is compatible with our value if the proton density is $\sim 10 \text{cm}^{-3}$ and lower than our value if the proton density is higher. The oxygen chemistry is included in the Meudon PDR code, and therefore we also derive $N(\text{OH}^+)$, $N(\text{H}_2\text{O}^+)$ and $N(\text{H}_3\text{O}^+)$ together with $N(\text{H}_3^+)$. In Table 7, we report these computed column densities for the best models matching H_3^+ observations toward J1747, for $n_{\text{H}} = 10, 20$, and

50 cm^{-3} , and compare them to the observed values toward Sgr B2(N) in the -130, -60 km s^{-1} velocity range. We find a very remarkable agreement. The $n_{\text{H}} = 50 \text{ cm}^{-3}$ model underestimates the observations only slightly. The computed column density of H_3O^+ is also compatible with the observations that are reported for the lowest (1,0) ortho level. So, our values of ζ deduced with H_3^+ observations are consistent with OH^+ , H_2O^+ and H_3O^+ observations as well.

A significant discrepancy between our models and Indriolo et al. (2015) results concerns the molecular fraction. Indriolo et al. (2012, 2015) estimate the molecular fraction using H_2O^+ main formation and destruction reactions



and they obtain:

$$f = \frac{2 x_e k_5 / k_3}{N(\text{OH}^+)/N(\text{H}_2\text{O}^+) - k_4 / k_3}. \quad (6)$$

The use of this expression relies on guesses of the electronic fraction and gas temperature. Equation 6 is used in Indriolo et al. (2015) to derive f in 105 diffuse gaseous components and leads to extremely small f values, lower than 0.1 for most components. For Sgr B2(N), in the -130, -60 km s^{-1} velocity component, Indriolo et al. (2015) obtain $f = 0.08 \pm 0.02$ whereas we find $f \sim 0.5 - 0.6$ for J1747.

The molecular fraction may also be directly derived from observations of H at 21 cm and estimate of $N(\text{H}_2)$ (Table 6). The column density of H is reported as $(1.03 \pm 0.3) \times 10^{21} \text{ cm}^{-2}$ in the -130, -60 km s^{-1} CMZ velocity component of the Sgr B2(N) line of sight by Indriolo et al. (2015), whereas Godard et al. (2012) report $N(\text{H}_2) = (2.0 \pm 0.5) \times 10^{21} \text{ cm}^{-2}$. We previously re-estimate this value to be $(9.4 \pm 1.5) \times 10^{20} \text{ cm}^{-2}$. The resulting molecular fraction is then 0.6 (0.8 with the Godard et al. (2012) estimate). These molecular fractions are then in very good agreement with those computed by the Meudon PDR code.

The origin of the discrepancy arises from the estimate of T and x_e . Indriolo et al. (2015) assume a gas temperature of 70 K and an electronic fraction of 1.5×10^{-4} , whereas the computed values in the PDR models that match J1747 and Sgr B2(N) observations are $\langle x_e \rangle = 1 - 2 \times 10^{-3}$ and $\langle T \rangle = 295$ to 391 K for n_{H} from 50 to 10 cm^{-3} . Using these values in Eq. 6 leads to $f \simeq 0.3-0.6$. These conflicting conclusions illustrate our discussion in Sect. 2 in which we highlight the risks of using speculated values in simple chemical analytic expressions, like Eqs. 4 or 6, especially in exotic conditions such as the Galactic center.

4.3. Heating and cooling mechanisms

Since the discovery of excited metastable H_3^+ in the CMZ, several authors tried to determine the energy source that heats the gas at a few hundred Kelvin (Yusef-Zadeh et al. 2013). Several hypothesis have been investigated: photoelectric effect, cosmic rays, X-rays, turbulence, or shocks.

Fig. 16 shows gas temperature, heating, and cooling rates versus the position (in A_V) for two models with $n_{\text{H}} = 100$

Table 7. Comparison of $N(\text{OH}^+)$, $N(\text{H}_2\text{O}^+)$ and $N(\text{H}_3\text{O}^+)$ observed toward Sgr B2(N) in the -130, -60 km s^{-1} velocity component to the computed values by the Meudon PDR code for the J1747 best models. Column densities for OH^+ and H_2O^+ are in 10^{14} cm^{-2} and in 10^{13} cm^{-2} for H_3O^+ . Cosmic-ray ionization rate is in 10^{-14} s^{-1} and size is in pc.

	Observations ^(a) Sgr B2(N)	Best models for J1747		
		10 cm^{-3}	20 cm^{-3}	50 cm^{-3}
ζ		1.0	2.6	5.0
L		45	22	7
$N(\text{OH}^+)$	7.5 ± 1.5	7.1	8.2	4.1
$N(\text{H}_2\text{O}^+)$	2.2 ± 0.4	2.3	2.4	1.6
$N(\text{H}_3\text{O}^+)$	4.0 ± 0.8	5.1	5.4	4.9

References. (a) Indriolo et al. (2015). The reported value of $N(\text{H}_3\text{O}^+)$ is for the (1,0) ortho level.

cm^{-3} illuminated on both sides by a radiation field that is ten times higher than the ISRF, with a metallicity $Z = 3$ and with, for the first model, $\zeta = 1 \times 10^{-16}$ and for the second model, $\zeta = 7 \times 10^{-14} \text{ s}^{-1}$. We see that for $\zeta = 10^{-16} \text{ s}^{-1}$, the only efficient heating mechanism is the photoelectric effect on grains. The temperature does not exceed 140 K and is not sufficient to excite H_3^+ as observed in CMZ conditions. On the contrary, for $\zeta = 7 \times 10^{-14} \text{ s}^{-1}$, cosmic-ray ionizations and exothermic chemical reactions ($\Delta E = 4.7 \text{ eV}$ for the $\text{H}_3^+ + \text{e}^-$ into the three H recombination channel) are efficient heating mechanisms through the whole cloud and keep the gas temperature at $T > 240 \text{ K}$. We find that our 4 eV injection per cosmic-ray H_2 ionization hypothesis is sufficient to heat the gas at temperatures around 250-300 K, consistent with H_3^+ excitation under CMZ conditions.

The major coolants are O and C^+ in the $\zeta = 10^{-16} \text{ s}^{-1}$ model. For the $\zeta = 7 \times 10^{-14} \text{ s}^{-1}$ model, cooling by H_2 starts to be important because of the high temperature. We find CO is not an important coolant in such diffuse gas because of a too low abundance.

4.4. Limits and hypothesis of our models

Our models have several limits. First, we use 1D isochoric PDR models. So, even though we account for detailed physical and chemical processes, the geometry is simplistic compared to reality. In particular, we assume only one H_3^+ component on each line of sight whereas HF absorption spectra show several components. For the J1747 line of sight, we tried a χ^2 minimization on subcomponents assuming the same repartition of H_3^+ as HF. Cosmic-ray ionization rates deduced this way are on the same order of magnitude as that obtained considering only a single component.

An important factor of our models is the efficient H_2 formation rate on PAHs. Our PDR models reproduce $N(\text{H}_3^+)$ and its excitation at high ζ because we assume H atoms can efficiently form H_2 on PAHs via the Eley-Rideal mechanism. The formation rate of H_2 on PAHs is not well known, but some recent experiments suggest the process is efficient on the edge sites of PAHs (Goumans & Bromley 2011; Boschman et al. 2012; Mennella et al. 2012). Moreover, ISO and Spitzer observations of H_2 emission lines in PDRs also suggest that

H₂ must be formed efficiently on PAHs (Habart et al. 2004, 2011). If the H₂ formation rate was lower than that computed in our models, the deduced cosmic-ray flux would be lower (see Fig. 7) and not efficient enough to heat the gas and explain H₃⁺ excitation. Then, other heating sources would have to be found. We tested several other possibilities, and none of them are satisfying. Increasing the UV flux to heat the gas by photoelectric effect on grains is not a good hypothesis as the photodissociation rate of H₂ becomes too high, such that it becomes difficult to reproduce the observed column densities. We also investigated the role of X-rays heating with a new version of the Meudon PDR code (Godard et al., in preparation). Several X-rays sources can be found in the Galactic center. X-rays emitted by the ionized gas in the central cavity have a flux that is too low to be responsible for the gas temperature in the CMZ (the most distant excited H₃⁺ detected by Goto et al. 2011 is at more than 100 pc of Sgr A*). Another candidate could be heating by turbulent energy dissipation. Thanks to their vortex model, the TDR code, Godard et al. (2014) suggested that intermittent turbulent energy dissipation may explain the presence of SH⁺ and CH⁺ observed by Herschel in the CMZ. Nevertheless, this process only heats a small fraction of the gas and may not be efficient enough to explain the global heating of the CMZ. Introducing this scenario for H₃⁺ would require a numerical model consistently taking both PDR physics and chemistry into account as well as turbulent energy dissipation effects on chemistry and H₃⁺ excitation. E. Bron (Bron 2014) developed a promising method to combine both approaches, based on the modeling of statistical properties of turbulence.⁶ We will test this method in a future study.

5. Conclusions

Our PDR models suggest a cosmic-ray ionization rate of H₂ in the CMZ of $\sim (1 - 11) \times 10^{-14} \text{ s}^{-1}$. The origin of this uncertainty range is due to the difficulty in constraining density from observations. This high value allows us to reproduce the observed column densities of H₃⁺ and its unusual excitation in the metastable state (3,3) observed toward nine lines of sight in the CMZ spanning ~ 100 pc apart from Sgr A*. The deduced cosmic-ray ionization rate is also compatible with the one deduced from synchrotron emission and Fe K α line emission (Yusef-Zadeh et al. 2013). As a bonus, we also reproduce $N(\text{OH}^+)$, $N(\text{H}_2\text{O}^+)$ and $N(\text{H}_3\text{O}^+)$ observed in the CMZ by Herschel toward Sgr B2(N), a line of sight close to one line of sight where H₃⁺ is detected. We confirm the suggestion by Oka & Epp (2004) that the gas probed by H₃⁺ observations in the CMZ is diffuse and warm. Indeed, PDR models matching observations have a proton density $\lesssim 100 \text{ cm}^{-3}$ and $T \sim 212\text{--}505 \text{ K}$. The main source of heating of the diffuse gas in the CMZ is the suprathermal electrons ejected from the gas by cosmic-ray ionizations and exothermic dissociative recombination reactions. If the analysis is only based on the J1747 line of sight, for which more constraints can be used, then models tend to favor gas densities that are lower than 50 cm^{-3} . In that case, sizes of the diffuse components probed by H₃⁺ are large (several ten parsecs to about 100 parsecs). This means that the diffuse gas probed by H₃⁺ spans the whole CMZ. This is in agreement with H₃⁺ observations that present the same behaviors in different directions in the CMZ.

We also show the importance of treating the detail of physical processes in astrochemical problems. We demonstrate how the simple analytic relationship between $N(\text{H}_3^+)$ and ζ (Eq. 4), commonly used to infer the cosmic-ray ionization rate in interstellar gas, may fail in an exotic medium. Indeed, for low and moderate cosmic-ray ionization rates the column density of H₃⁺ increases linearly with ζ but decreases at high ζ , in contradiction with the analytic expression. This is due to the ionization of H and H₂ by cosmic rays, which reduces the molecular fraction of the gas and increases the electronic fraction of the gas leading to fast H₃⁺ recombination.

A key parameter of our results concerns the H₂ formation rate. We reached the conclusion that the H₂ formation rate in the diffuse gas of the CMZ must be enhanced when compared to local diffuse clouds. Indeed, in the CMZ, as in PDRs, the warm temperature of the gas opens the possibility of efficiently forming H₂ on grains and PAHs via chemisorption of H atoms followed by Eley-Rideal mechanism. Therefore, on one hand, a high cosmic-ray ionization rate reduces the number of available H atoms to form H₂ since they are ionized in H⁺. On the other hand, heating the gas to several hundred Kelvin, cosmic rays open the efficient H₂ formation route via chemisorption sites. This allows us to reach high column densities of H₃⁺ at large cosmic-ray ionization rates.

Acknowledgements. We thank Octavio Roncero who made the H₃⁺-H₂ collision rates available to us. We thank Takeshi Oka for useful discussions about H₃⁺ and CO in the central molecular zone. Exchanges with Farhad Yusef-Zadeh and Vincent Tatischeff are acknowledged for their assistance in deriving the cosmic-ray ionization rate from synchrotron emission. We also thank Mickaël Coriat for his help concerning high energy astrophysics and radio counterpart as well as Thibaut Paumard for useful discussions about the Galactic center. This work was supported in part by grant SYMPATICO (ANR-11-BS56-0023) from the French Agence Nationale de la Recherche. It was also supported by the French CNRS national program PCMI. Maxime Ruaud acknowledges funding by the European Research Council (Starting Grant 3DICE, grant agreement 336474).

References

- Abia, C., Cunha, K., Cristallo, S., & de Laverny, P. 2015, ArXiv e-prints
- Aguado, A., Barragán, P., Prossimi, R., et al. 2010, *J. Chem. Phys.*, 133, 024306
- Bialy, S. & Sternberg, A. 2015, *MNRAS*, 450, 4424
- Boschman, L., Reitsma, G., Cazaux, S., et al. 2012, *ApJ*, 761, L33
- Brittain, S. D., Simon, T., Kulesa, C., & Rettig, T. W. 2004, *ApJ*, 606, 911
- Bron, E. 2014, PhD thesis, Université Paris Diderot
- Bron, E., Le Bourlot, J., & Le Petit, F. 2014, *A&A*, 569, A100
- Compiègne, M., Verstraete, L., Jones, A., et al. 2011, *A&A*, 525, A103
- Daffon, S. & Cunha, K. 2004, *ApJ*, 617, 1115
- Draine, B. T. & Li, A. 2007, *ApJ*, 657, 810
- Faure, A. & Tennyson, J. 2003, *MNRAS*, 340, 468
- Faure, A., Wiesenfeld, L., Valiron, P., & et al. 2006, *Royal Society of London Philosophical Transactions Series A*, 364, 3113
- Federman, S. R., Weber, J., & Lambert, D. L. 1996, *ApJ*, 463, 181
- Felenbok, P. & Roueff, E. 1996, *ApJ*, 465, L57
- Fitzpatrick, E. L. & Massa, D. 1986, *ApJ*, 307, 286
- Flower, D. R. & Pineau des Forêts, G. 1998, *MNRAS*, 297, 1182
- Geballe, T. R. 2012, *Royal Society of London Philosophical Transactions Series A*, 370, 5151
- Geballe, T. R., Goto, M., Usuda, T., Oka, T., & McCall, B. J. 2006, *ApJ*, 644, 907
- Geballe, T. R., McCall, B. J., Hinkle, K. H., & Oka, T. 1999, *ApJ*, 510, 251
- Geballe, T. R. & Oka, T. 1996, *Nature*, 384, 334
- Geballe, T. R. & Oka, T. 2010, *ApJ*, 709, L70
- Gerin, M., de Luca, M., Black, J., et al. 2010a, *A&A*, 518, L110
- Gerin, M., de Luca, M., Goicoechea, J. R., et al. 2010b, *A&A*, 521, L16
- Gibb, E. L., Brittain, S. D., Rettig, T. W., et al. 2010, *ApJ*, 715, 757
- Godard, B., Falgarone, E., Gerin, M., et al. 2012, *A&A*, 540, A87
- Godard, B., Falgarone, E., & Pineau des Forêts, G. 2014, *A&A*, 570, A27
- Gómez-Carrasco, S., González-Sánchez, L., Aguado, A., et al. 2012, *J. Chem. Phys.*, 137, 094303

⁶ Available at <https://tel.archives-ouvertes.fr/tel-01111148>

- Gonzalez Garcia, M., Le Bourlot, J., Le Petit, F., & Roueff, E. 2008, *A&A*, 485, 127
- Goto, M., Geballe, T. R., Indriolo, N., et al. 2014, *ApJ*, 786, 96
- Goto, M., Indriolo, N., Geballe, T. R., & Usuda, T. 2013, *Journal of Physical Chemistry A*, 117, 9919
- Goto, M., McCall, B., Geballe, T., Usuda, T., & Oka, T. 2005, in *High Resolution Infrared Spectroscopy in Astronomy*, ed. H. U. Käufl, R. Siebenmorgen, & A. Moorwood, 244–247
- Goto, M., McCall, B. J., Geballe, T. R., et al. 2002, *PASJ*, 54, 951
- Goto, M., Usuda, T., Geballe, T. R., et al. 2011, *PASJ*, 63, L13
- Goto, M., Usuda, T., Nagata, T., et al. 2008, *ApJ*, 688, 306
- Goumans, T. P. M. & Bromley, S. T. 2011, *MNRAS*, 414, 1285
- Grenier, I. A., Black, J. H., & Strong, A. W. 2015, *ARA&A*, 53, 199
- Gry, C., Boulanger, F., Nehmé, C., et al. 2002, *A&A*, 391, 675
- Habart, E., Abergel, A., Boulanger, F., et al. 2011, *A&A*, 527, A122
- Habart, E., Boulanger, F., Verstraete, L., Walmsley, C. M., & Pineau des Forêts, G. 2004, *A&A*, 414, 531
- Hartquist, T. W., Black, J. H., & Dalgarno, A. 1978, *MNRAS*, 185, 643
- Hugo, E., Asvany, O., & Schlemmer, S. 2009, *J. Chem. Phys.*, 130, 164302
- Indriolo, N., Blake, G. A., Goto, M., et al. 2010, *ApJ*, 724, 1357
- Indriolo, N., Geballe, T. R., Oka, T., & McCall, B. J. 2007, *ApJ*, 671, 1736
- Indriolo, N. & McCall, B. J. 2012, *ApJ*, 745, 91
- Indriolo, N., Neufeld, D. A., Gerin, M., et al. 2012, *ApJ*, 758, 83
- Indriolo, N., Neufeld, D. A., Gerin, M., et al. 2015, *ApJ*, 800, 40
- Jura, M. 1974, *ApJ*, 191, 375
- Kokoouline, V., Faure, A., Tennyson, J., & Greene, C. H. 2010, *MNRAS*, 405, 1195
- Le Bourlot, J., Le Petit, F., Pinto, C., Roueff, E., & Roy, F. 2012, *A&A*, 541, A76
- Le Petit, F., Barzel, B., Biham, O., Roueff, E., & Le Bourlot, J. 2009, *A&A*, 505, 1153
- Le Petit, F., Nehmé, C., Le Bourlot, J., & Roueff, E. 2006, *ApJS*, 164, 506
- Le Petit, F., Roueff, E., & Herbst, E. 2004, *A&A*, 417, 993
- Lindsay, C. M. & McCall, B. J. 2001, *Journal of Molecular Spectroscopy*, 210, 60
- Lis, D. C., Schilke, P., Bergin, E. A., & Emprechtinger, M. 2012, *Royal Society of London Philosophical Transactions Series A*, 370, 5162
- Lis, D. C., Schilke, P., Bergin, E. A., et al. 2014, *ApJ*, 785, 135
- Liszt, H. 2003, *A&A*, 398, 621
- Liszt, H. S. 2006, *Royal Society of London Philosophical Transactions Series A*, 364, 3049
- Mathis, J. S., Mezger, P. G., & Panagia, N. 1983, *A&A*, 128, 212
- Mathis, J. S., Rimpl, W., & Nordsieck, K. H. 1977, *ApJ*, 217, 425
- McCall, B. J., Geballe, T. R., Hinkle, K. H., & Oka, T. 1998, *Science*, 279, 1910
- McCall, B. J., Geballe, T. R., Hinkle, K. H., & Oka, T. 1999, *ApJ*, 522, 338
- McCall, B. J., Hinkle, K. H., Geballe, T. R., et al. 2002, *ApJ*, 567, 391
- McCall, B. J., Huneycutt, A. J., Saykally, R. J., et al. 2003, *Nature*, 422, 500
- Mennella, V., Hornekær, L., Thrower, J., & Accolla, M. 2012, *ApJ*, 745, L2
- Meyer, D. M., Cardelli, J. A., & Sofia, U. J. 1997, *ApJ*, 490, L103
- Meyer, D. M., Jura, M., & Cardelli, J. A. 1998, *ApJ*, 493, 222
- Moskalenko, I. V., Porter, T. A., & Strong, A. W. 2006, *ApJ*, 640, L155
- Neufeld, D. A., Goicoechea, J. R., Sonnentrucker, P., et al. 2010, *A&A*, 521, L10
- Neufeld, D. A., Wolfire, M. G., & Schilke, P. 2005, *ApJ*, 628, 260
- Oka, T. 2013, *Chemical Reviews*, 113, 8738
- Oka, T. 2015, in *American Institute of Physics Conference Series*, Vol. 1642, American Institute of Physics Conference Series, 373–376
- Oka, T. & Epp, E. 2004, *ApJ*, 613, 349
- Oka, T., Geballe, T. R., Goto, M., Usuda, T., & McCall, B. J. 2005, *ApJ*, 632, 882
- Oka, T., Onodera, Y., Nagai, M., et al. 2012, *ApJS*, 201, 14
- Park, K. & Light, J. C. 2007, *J. Chem. Phys.*, 126, 044305
- Porter, T. A. & Strong, A. W. 2005, *International Cosmic Ray Conference*, 4, 77
- Rachford, B. L., Snow, T. P., Tumlinson, J., et al. 2002, *ApJ*, 577, 221
- Rolleston, W. R. J., Smartt, S. J., Dufton, P. L., & Ryans, R. S. I. 2000, *A&A*, 363, 537
- Roueff, E. 1996, *MNRAS*, 279, L37
- Rudolph, A. L., Fich, M., Bell, G. R., et al. 2006, *ApJS*, 162, 346
- Savage, B. D. & Sembach, K. R. 1996, *ARA&A*, 34, 279
- Schilke, P., Comito, C., Müller, H. S. P., et al. 2010, *A&A*, 521, L11
- Schilke, P., Lis, D. C., Bergin, E. A., Higgins, R., & Comito, C. 2013, *Journal of Physical Chemistry A*, 117, 9766
- Seaton, M. J. 1979, *MNRAS*, 187, 73P
- Snow, T. P., Destree, J. D., & Jensen, A. G. 2007, *ApJ*, 655, 285
- Sternberg, A., Le Petit, F., Roueff, E., & Le Bourlot, J. 2014, *ApJ*, 790, 10
- Strong, A. W., Porter, T. A., Digel, S. W., et al. 2010, *ApJ*, 722, L58
- Wakelam, V., Herbst, E., Loison, J.-C., et al. 2012, *ApJS*, 199, 21
- Yusef-Zadeh, F., Hewitt, J. W., Wardle, M., et al. 2013, *ApJ*, 762, 33

Table 5. Results of the best models defined as those minimizing χ^2 for the various densities, $n_H = 10, 20, 50$, and 100 cm^{-3} . Cosmic-ray ionization rates, ζ , are in 10^{-14} s^{-1} and sizes, L , in parsecs. Computed H_3^+ column densities, $N(J, K)$, are in 10^{14} cm^{-2} . The last three columns present computed molecular fractions, mean gas temperatures in Kelvin, and mean electronic fractions in 10^{-3} .

$n_H = 10 \text{ cm}^{-3}$										
Source	ζ	L	χ^2	N(1,1)	N(1,0)	N(3,3)	N(2,2)	f	$\langle T \rangle$	$\langle x_e \rangle$
GC IRS 21	1	94	0.6	19.5	11.5	12.8	0.14	0.5	316	1.3
GC IRS 3	3	108	0.3	9.6	4.4	9.4	0.11	0.4	471	3.0
GC IRS 1W	1	81	0.3	15.8	9.2	10.4	0.11	0.5	321	1.4
GCS 3-2	3	121	4.79	11.0	5.0	10.9	0.13	0.4	467	3.0
J1743	0.3	74	0.006	13.0	8.8	5.0	0.05	0.7	212	0.6
J1747	1	45	0.004	5.8	3.1	4.3	0.05	0.5	391	1.7
NHS 21	1	53	0.2	7.9	4.4	5.5	0.06	0.5	354	1.5
NHS 22	1	78	0.08	14.8	8.6	9.7	0.11	0.5	323	1.4
NHS 25	3	108	0.08	9.6	4.4	9.5	0.11	0.3	474	3.0
NHS 42	0.7	76	0.1	15.8	9.9	8.6	0.09	0.6	278	1.0
Mean	1	66	0.5	11.2	6.4	7.5	0.08	0.5	337	1.4
$n_H = 20 \text{ cm}^{-3}$										
Source	ζ	L	χ^2	N(1,1)	N(1,0)	N(3,3)	N(2,2)	f	$\langle T \rangle$	$\langle x_e \rangle$
GC IRS 21	3	51	0.37	22.0	12.6	17.0	0.35	0.5	319	1.3
GC IRS 3	6	61	0.46	10.1	4.5	11.1	0.25	0.4	472	3.0
GC IRS 1W	3	41	0.19	17.0	9.8	12.9	0.26	0.5	315	1.3
GCS 3-2	3	34	4.90	12.8	7.3	9.7	0.20	0.5	320	1.4
J1743	0.6	33	0.01	12.5	8.6	4.9	0.10	0.7	187	0.6
J1747	3	22	0.21	6.6	3.6	5.2	0.11	0.5	337	1.6
NHS 21	2	25	0.17	8.4	4.7	6.3	0.13	0.5	320	1.4
NHS 22	2	37	0.15	15.8	9.3	11.1	0.23	0.6	299	1.2
NHS 25	3	29	0.07	10.4	5.9	7.9	0.17	0.5	321	1.4
NHS 42	1	35	0.14	16.2	10.5	8.7	0.18	0.6	238	0.8
Mean	3	33	0.08	12.2	6.9	9.3	0.19	0.5	321	1.4
$n_H = 50 \text{ cm}^{-3}$										
Source	ζ	L	χ^2	N(1,1)	N(1,0)	N(3,3)	N(2,2)	f	$\langle T \rangle$	$\langle x_e \rangle$
GC IRS 21	12	24	0.1	16.0	8.0	17.7	0.84	0.4	432	2.1
GC IRS 3	12	12	0.5	7.0	3.5	7.7	0.37	0.4	424	2.2
GC IRS 1W	6	14	0.2	16.5	9.9	13.1	0.59	0.6	302	1.1
GCS 3-2	12	15	4.4	9.4	4.7	10.4	0.50	0.4	426	2.1
J1743	3	10	0.2	12.1	8.0	6.6	0.31	0.7	220	0.7
J1747	5	7	0.1	6.4	3.8	4.9	0.23	0.6	295	1.2
NHS 21	5	8	0.2	7.9	4.7	6.1	0.28	0.6	295	1.2
NHS 22	5	12	0.2	14.9	9.2	10.7	0.49	0.6	278	1.0
NHS 25	6	9	0.1	9.9	5.8	7.8	0.36	0.5	303	1.2
NHS 42	3	12	0.1	15.6	1.0	8.8	0.41	0.7	227	0.7
Mean	6	11	0.1	12.1	7.2	9.5	0.44	0.6	301	1.1
$n_H = 100 \text{ cm}^{-3}$										
Source	ζ	L	χ^2	N(1,1)	N(1,0)	N(3,3)	N(2,2)	f	$\langle T \rangle$	$\langle x_e \rangle$
GC IRS 21	11	7	0.5	18.6	11.4	15.9	1.3	0.6	310	1.0
GC IRS 3	30	8	1.1	7.7	3.7	10.2	0.88	0.4	505	2.6
GC IRS 1W	10	6	0.4	14.8	9.3	12.0	0.97	0.6	294	1.0
GCS 3-2	11	4	7.0	11.0	6.8	9.0	0.74	0.6	297	1.0
J1743	3	5	0.04	12.9	9.7	4.9	0.44	0.7	160	0.4
J1747	9	3	0.2	6.1	3.8	4.7	0.40	0.6	277	1.0
NHS 21	10	3	0.3	7.4	4.6	5.9	0.50	0.6	286	1.0
NHS 22	8	5	0.1	14.1	9.2	9.8	0.80	0.6	256	0.8
NHS 25	11	4	0.1	8.9	5.5	7.3	0.60	0.6	293	1.0
NHS 42	6	5	0.2	15.1	10.2	9.3	0.77	0.7	233	0.7
Mean	11	4	0.07	10.5	6.4	8.9	0.73	0.6	307	1.1

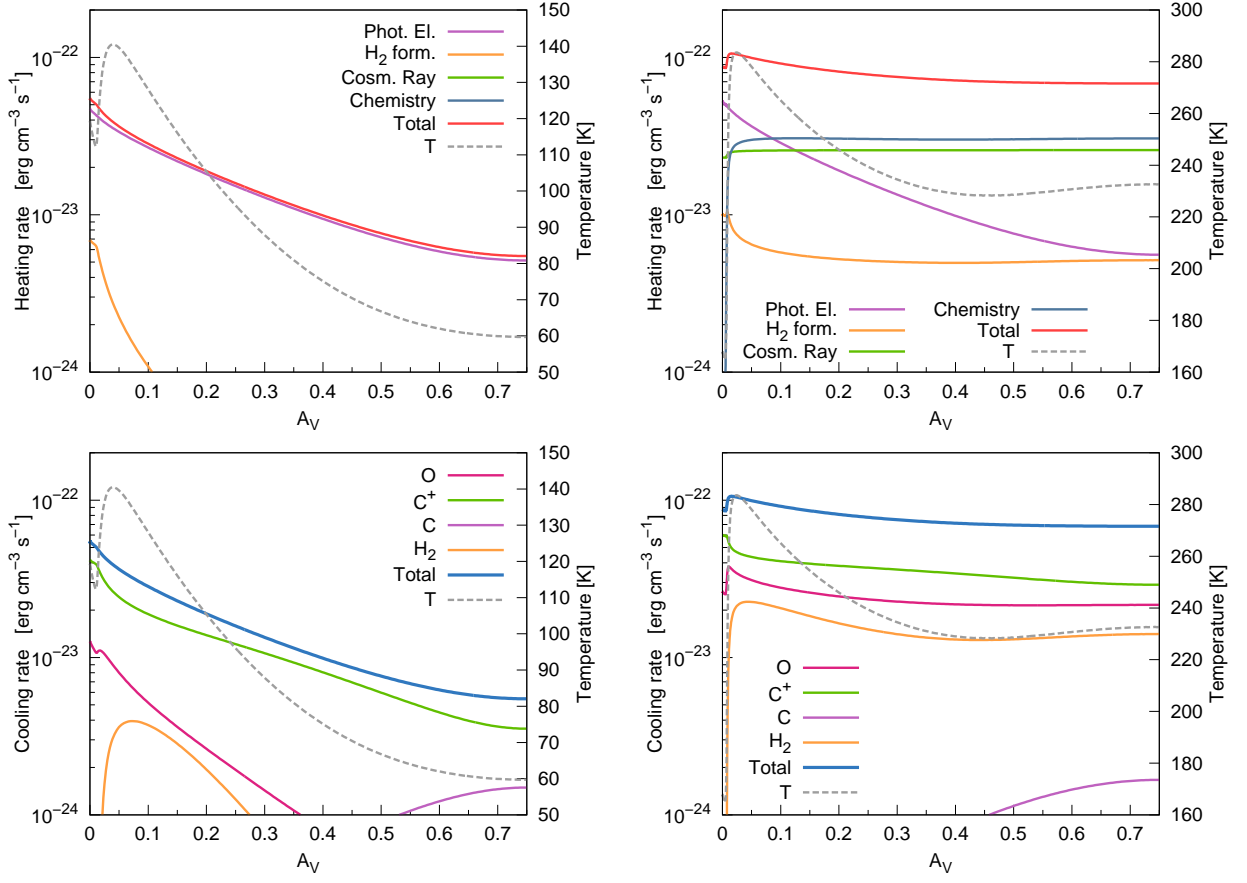


Fig. 16. Heating (top panels) and cooling (bottom panels) rates as a function of visual extinction for two models (left: $\zeta = 10^{-16} \text{ s}^{-1}$; right: $\zeta = 7 \times 10^{-14} \text{ s}^{-1}$). In both models, $n_{\text{H}} = 100 \text{ cm}^{-3}$, $G_0 = 10$ and, on both sides of the clouds, $A_V^{\text{max}} = 1.5$, $Z = 3$. Figures present profiles from the edge of the cloud to the center. Cosmic ray heating and heating by exothermic reactions do not appear for the $\zeta = 10^{-16} \text{ s}^{-1}$ model because their rate is always lower than $10^{-24} \text{ erg cm}^{-3} \text{ s}^{-1}$.